

Spatially Non-Stationary XL-MIMO Channel Estimation: A Three-Layer Generalized Approximate Message Passing Method

Anzheng Tang*, Jun-Bo Wang*, Yijin Pan*, Wence Zhang[†], Xiaodan Zhang[‡],
Yijian Chen[§], Hongkang Yu[§], and Rodrigo C. de Lamare[¶]

Abstract—In this paper, channel estimation problem for extremely large-scale multi-input multi-output (XL-MIMO) systems is investigated with the considerations of the spherical wavefront effect and the spatially non-stationary (SnS) property. Due to the diversities of SnS characteristics among different propagation paths, the concurrent channel estimation of multiple paths becomes intractable. To address this challenge, we propose a two-phase channel estimation scheme. In the first phase, the angles of departure (AoDs) on the user side are estimated, and a carefully designed pilot transmission scheme enables the decomposition of the received signal from different paths. In the second phase, the subchannel estimation corresponding to different paths is formulated as a three-layer Bayesian inference problem. Specifically, the first layer captures block sparsity in the angular domain, the second layer promotes SnS property in the antenna domain, and the third layer decouples the subchannels from the observed signals. To efficiently facilitate Bayesian inference, we propose a novel three-layer generalized approximate message passing (TL-GAMP) algorithm based on structured variational message passing and belief propagation rules. Simulation results validate the convergence and effectiveness of the proposed algorithm, showcasing its robustness to different channel scenarios.

Index Terms—XL-MIMO systems, SnS property, channel estimation, approximate message passing.

I. INTRODUCTION

With the advancement of wireless communication technology and the growing demand for higher data rates, it is anticipated that the number of antennas and the array aperture will significantly exceed those used in existing massive multiple-input-multiple-output (MIMO) systems [1], [2]. This trend has given rise to the concept of extremely large-scale MIMO (XL-MIMO) [3], [4], which involves deploying an exceptionally large number of antennas in a compact space with a discrete

or even continuous aperture [5], [6]. Thanks to the substantial beamforming gain and vast spatial degrees of freedom (DoF), XL-MIMO is considered a promising technology for beyond 5G and 6G communications.

In XL-MIMO systems, the significant increase in the array aperture results in near-field transmission [4], [5], [7]–[9]. Consequently, various channel characteristics, not typically considered in conventional massive MIMO systems, require exploration, for example, the spherical wavefront effect and SnS property. Specifically, the large-aperture antenna array leads to a non-negligible Rayleigh distance. As a result, the plane wavefront assumption becomes inapplicable to near-field XL-MIMO channels, and instead, the spherical wavefront effects should be considered [10], [11]. Moreover, the extremely large array aperture introduces the SnS property along the array. Intuitively, different portions of the array could observe the propagation environment from different perspectives, implying that the array elements can capture the signal from a certain propagation path but with varying powers. To quantitatively characterize the SnS property, the visibility region (VR)-based channel modeling method is widely adopted in XL-MIMO systems [12]–[16]. Considering both the near-field effect and SnS property, the problem of channel estimation for XL-MIMO systems becomes much more difficult.

A. Related Works

While a number of methods have been proposed to estimate the channels in XL-MIMO systems, most of them only apply to spatially stationary channel models [17]–[21]. To address the SnS estimation problem, [22] proposed subarray-wise and scatterer-wise estimation schemes. However, these schemes were heuristic and did not fully exploit the inherent structure of the XL-MIMO channels, such as potential characteristics in the antenna or angular domains. Moreover, based on the assumption of subarray-wise VRs, [23] proposed a group time block code (GTBC) based signal extraction scheme for each subarray in [23]. Subsequently, the SnS channel estimation was transformed into several spatially stationary estimation tasks. Nevertheless, the method overlooked the spatial correlation among subarrays, and the subarray-wise VR assumption may be idealistic, as users or scatterers might only have visibility to a portion of array elements in each subarray. Additionally, in the context of SnS reconfigurable intelligent surface (RIS) cascaded channels, a three-step channel estimation and VR detection scheme was proposed in [12],

Anzheng Tang, Jun-bo Wang and Yijin Pan are with the National Mobile Communications Research Laboratory, Southeast University, Nanjing 210096, China. (email: {anzhengt, jbwang, and panyj}@seu.edu.cn)

Wence Zhang is with the School of Computer Science and Communication Engineering and the Jiangsu Key Laboratory of Security Technology for Industrial Cyberspace, Jiangsu University, Zhenjiang 212013, China. (e-mail: wencezhang@ujs.edu.cn)

Xiaodan Zhang is with the School of Management, Shenzhen Institute of Information Technology, Shenzhen 518172, China. (e-mail: Danyzxd@163.com)

Yijian Chen and Hongkang Yu are with the Wireless Product Research and Development Institute, ZTE Corporation, Shenzhen 518057, China. (e-mail: {yu.hongkang, chen.yijian}@zte.com.cn)

Rodrigo C. de Lamare is with the Centre for Telecommunications Studies, Pontifical Catholic University of Rio de Janeiro, Rio de Janeiro 22451-900, Brazil, and also with the Department of Electronic Engineering, University of York, York YO10 5DD, U.K. (e-mail: delamare@puc-rio.br).

where the VR detection method, relying on receive signal power, is contingent on the accuracy of channel estimation and is sensitive to noise levels. Particularly, in low signal-to-noise ratio (SNR) scenarios, this approach may suffer severe performance degradation. Furthermore, the method becomes impractical when considering multipath propagation between the RIS and users.

Considering the inherent antenna-domain or delay-domain sparsity in SnS channels, various Bayesian inference-based methods have been proposed. Exploiting delay-domain sparsity, [24] introduced an adaptive grouping sparse Bayesian learning (AGSBL) scheme for uplink channel estimation. Utilizing antenna-domain sparsity resulting from the SnS property, [25] characterized the XL-MIMO channel with a subarray-wise Bernoulli-Gaussian distribution. Subsequently, a bilinear message passing (MP) algorithm was developed for joint user activity detection and channel estimation in the presence of the SnS property. To simultaneously capture antenna- and delay-domain sparsity, [26] proposed a structured prior model with the hidden Markov model (HMM) to capture the characteristics of VR and delay domain clustering. While these contributions primarily focused on characterizing antenna-domain or delay-domain channels using statistical distributions such as mean and variance, they overlooked essential propagation characteristics, which potentially lead to a degradation in estimation performance.

To address the aforementioned issues, [27] proposed to jointly utilize the sparse properties of channels in the polar domain and VR vectors and developed a joint channel estimation and VR detection algorithm based on the fast sparse Bayesian learning (FSBL) framework. However, the FSBL-based method involved matrix inversion operations in each iteration, resulting in extremely high computational complexity. Furthermore, in our previous work [28], we proposed a two-stage VR detection and channel estimation scheme based on message passing (MP) and orthogonal matching pursuit (OMP), considering the antenna-domain and angular-domain characteristics. Nervelessness, a notable drawback of this method is the manual separation of the two stages, leading to inadequate utilization of angular-domain information during the VR detection stage. Additionally, it is worth mentioning that the aforementioned estimation methods are developed in the context of a multiple-input-single-output (MISO) scenario, and direct extension to the MIMO scenario is not feasible.

B. Main Contributions

In this paper, we study the XL-MIMO channel estimation problem, considering the user equipped with multiple antennas and accounting for spherical wavefront effects and SnS property. Given the distinct characteristics inherent in various propagation paths, the concurrent estimation of multiple paths poses a significant challenge. To this end, we present a two-phase channel estimation scheme. The main contributions can be summarized as follows:

- We propose a two-phase channel estimation scheme tailored for the SnS XL-MIMO channel estimation problem. Specifically, in the first phase, the AoDs on the user side

are estimated, and a carefully designed pilot transmission scheme enables the decomposition of the received signal from different SnS paths. In the second phase, the subchannel estimation corresponding to different paths is estimated.

- To solve the cascaded estimation of VRs and channels coefficients, we formulate the subchannels estimation as a three-layer Bayesian inference problem. To be specific, in the first layer, the goal is to capture the block sparsity of the SnS channel within the angular domain. The second layer focuses on capturing the SnS property in the antenna domain. Moving forward, the third layer facilitates the decoupling of subchannels from the observed signal.
- To efficiently achieve Bayesian inference, we propose a computationally efficient three-layer generalized message-passing (TL-GAMP) algorithm by combining structured variational message passing and belief propagation rules. Additionally, in the first and third layers, we simplify the message calculations by omitting certain infinitesimal terms, thereby significantly reducing computational complexity.
- In comparison to existing baselines, the proposed channel estimation algorithm demonstrates superior performance due to the joint exploitation of angular-domain and antenna-domain characteristics. Meanwhile, the algorithm demonstrates remarkable robustness in handling different channel scenarios.

C. Organization and Notations

Organization: The rest of this paper is organized as follows. In Section II, we introduce the system model. Section III presents a two-phase channel estimation scheme. In Section IV, the subchannel estimation problem is formulated as a three-layer generalized bilinear inference problem, and a computationally effective algorithm is proposed. Simulations are carried out in Section V. Finally, conclusions are drawn in Section VI.

Notations: lower-case letters, bold-face lower-case letters, and bold-face upper-case letters are used for scalars, vectors and matrices, respectively; The superscripts $(\cdot)^T$ and $(\cdot)^H$ stand for transpose and conjugate transpose, respectively; $\text{diag}(x_1, x_2, \dots, x_N)$ denotes a diagonal matrix with $\{x_1, x_2, \dots, x_N\}$ being its diagonal elements; $\text{blkdiag}(\mathbf{X}_1, \mathbf{X}_2, \dots, \mathbf{X}_N)$ denotes a block diagonal matrix with $\{\mathbf{X}_1, \mathbf{X}_2, \dots, \mathbf{X}_N\}$ being its diagonal elements; $\mathbb{C}^{M \times N}$ denotes an $M \times N$ complex matrix. In addition, a random variable $x \in \mathbb{C}$ drawn from the complex Gaussian distribution with mean m and variance v is characterized by the probability density function (PDF) $\mathcal{CN}(x; m, v) = \exp\{-|x - m|^2/v\}/\pi v$; a random variable $\gamma \in \mathbb{R}$ from Gamma distribution with mean a/b and variance a/b^2 is characterized by the PDF $\mathcal{G}a(\gamma; a, b) = \gamma^{a-1} \exp(-\gamma b)$; $m_{n_a \rightarrow n_b}(x)$ indicates a message passed from node n_a to node n_b .

II. SYSTEM MODEL

Consider a narrowband millimeter-wave (mmWave) XL-MIMO system, where the time-division duplexing (TDD) mode is adopted. As depicted in Fig. 1, a BS with N_R antennas

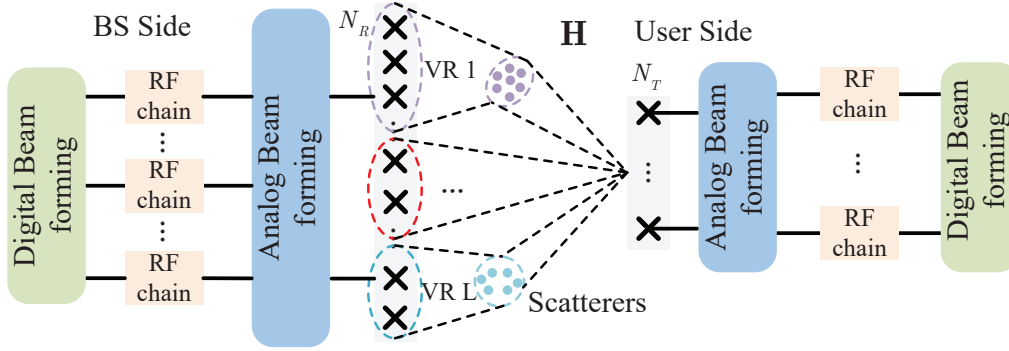


Fig. 1. Illustration of mmWave XL-MIMO system with a hybrid beamforming architecture.

and N_{RF} radio frequency (RF) chains serves a user¹ with $N_T \ll N_R$ antennas. Without loss of generality, we assume that the transceivers are arranged with uniform linear arrays (ULAs), and the antenna spacing is denoted by $d = \lambda/2$, where λ indicates the carrier wavelength. The set of BS antenna elements is given by $\mathcal{N} = \{1, 2, \dots, N_R\}$.

The large-aperture antenna array on the BS side results in a more significant Rayleigh distance, placing the user in the near-field region of the BS. Consequently, the assumption of the plane wavefront, commonly employed in far-field communications, becomes inapplicable [7]. Furthermore, with the increase in array aperture, the presence of obstacles and incomplete scattering in wireless propagation environments introduces the SnS property along the array on the BS side [12], [14]–[16].

To account for the spherical wavefront effect and the SnS property, we employ a single-side near-field model to characterize the uplink channel $\mathbf{H} \in \mathbb{C}^{N_T \times N_R}$, which can be represented as [14], [26]

$$\mathbf{H} = \sqrt{N_T N_R} \sum_{l=1}^L g_l (\mathbf{s}_l \odot \mathbf{a}_R(\vartheta_l, r_l)) \mathbf{a}_T^H(\psi_l), \quad (1)$$

where L is the number of propagation paths, and when $l = 1$, it refers to the line-of-sight (LoS) path, while $l > 1$ indicates non-line-of-sight (NLoS) paths; g_l represents the l -th complex path gain; $\mathbf{s}_l = [s_{l,1}, s_{l,2}, \dots, s_{l,N_R}]^T \in \mathbb{Z}^{N_R \times 1}$ is the visibility indicator vector of the l -th path; \odot indicates the Hadamard product. If the l -th propagation path is spatially stationary, \mathbf{s}_l is represented as an all-one vector, i.e., $\mathbf{s}_l = \mathbf{1}_{N_R \times 1}$. Conversely, if the l -th path is SnS, the n -th entry of \mathbf{s}_l is modeled as [12], [14], [28]

$$s_{l,n} = \begin{cases} 1, & \text{if } n \in \varphi_l, \\ 0, & \text{otherwise.} \end{cases} \quad (2)$$

where set $\varphi_l \subseteq \mathcal{N}$ denotes the VR for the l -th path, i.e., the l -th path is visible to elements in φ_l , and is invisible to the elements outside φ_l . Moreover, we define $\phi_l = |\varphi_l|/N_R$, indicating the proportion of visible elements to the l -th path, where $|\varphi_l|$ denotes the cardinality of the set φ_l . The parameters ϑ_l and r_l denote the angle of arrival (AOA) on the BS side and the distance between the reference antenna element on the BS side

and the scatterers or user in the l -th path, respectively. Without loss of generality, we consider the first antenna element as the reference element. Additionally, ψ_l represents AoD of the user in the l -th path. Finally, $\mathbf{a}_T(\psi_l) \in \mathbb{C}^{N_T \times 1}$ and $\mathbf{a}_R(\vartheta_l, r_l) \in \mathbb{C}^{N_R \times 1}$ are respectively the far-field and near-field array steering vectors at the user and BS sides, which are respectively given by

$$\mathbf{a}_T(\psi_l) = \frac{1}{\sqrt{N_T}} [1, \dots, e^{-j\frac{2\pi}{\lambda}(N_T-1)d \sin \psi_l}]^T, \quad (3)$$

$$\mathbf{a}_R(\vartheta_l, r_l) = \frac{1}{\sqrt{N_R}} [e^{j\frac{2\pi}{\lambda} \Delta_{l,1}}, \dots, e^{j\frac{2\pi}{\lambda} \Delta_{l,N_R}}]^T, \quad (4)$$

where $\Delta_{l,n} = -d(n-1) \sin \vartheta_l + d^2(n-1)^2 \cos^2 \vartheta_l / (2r_l)$ is the wave path difference between the n -th element and the reference element for the l -th path.

III. TWO-PHASE ESTIMATION SCHEME

Due to the channel reciprocity in TDD mode, the estimation of the uplink channel is sufficient [29]. Meanwhile, considering that the channels are block-fading, the channel parameters remain constant within each coherence block. Assume that each coherence block is divided into several consecutive subframes, and P consecutive subframes are utilized for the channel estimation task with each subframe further divided into K time slots. In each uplink subframe, the user only activates a single RF chain to transmit the pilot signal on one beam while the BS combines the received pilot signal using all RF chains associated with different beams [30]. Specifically, the BS utilizes K time slots to traverse all received beams. Subsequently, the user changes the transmit beam every K time slots, as depicted in Fig. 2.

Given that each propagation path exhibits different SnS property, the concurrent estimation of multipath presents a significant challenge. To tackle this issue, we propose a two-phase estimation scheme in this paper. In the first phase, the AoDs can be initially estimated. According to the obtained AoDs, the user can select a suitable transmit beam aligned with the AoDs. This allows the BS to effectively decouple the received signals from multipaths. Moving to the second phase, we proceed to estimate the remaining path parameters. Finally, through the superposition of all paths, we obtain the complete channel information. In the following, we will elaborate on the details of the two-phase estimation scheme.

¹Notably, considering the orthogonal pilots for different user, the proposed estimation scheme can be straightforwardly extended to multi-user scenario.

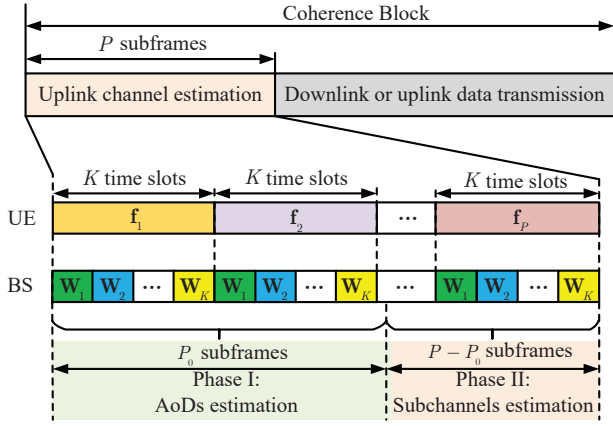


Fig. 2. Two-phase uplink channel estimation scheme.

1) *Stage I: AoDs Estimation*: In the first phase, as the channel parameters are unknown, both the user and BS randomly select transmit and combiner beams from predefined codebooks. Let $\mathbf{f}_p \in \mathbb{C}^{N_T \times 1}$ represent the transmit beam in the p -th subframe, and $\mathbf{W}_k \in \mathbb{C}^{N_R \times N_{RF}}$ denotes the combiner matrix for the k -th time slot in the p -th subframe. Mathematically, the received pilot signal $\mathbf{y}_{p,k} \in \mathbb{C}^{N_{RF} \times 1}$ at the BS in the k -th time slot of the p -th subframe is given by

$$\mathbf{y}_{p,k} = \mathbf{W}_k^H \mathbf{H} \mathbf{f}_p s_{p,k} + \mathbf{W}_k^H \mathbf{n}_{p,k}, \quad (5)$$

where $s_{p,k} \in \mathbb{C}$ and $\mathbf{n}_{p,k} \sim \mathcal{CN}(\mathbf{n}_{p,k}; 0, \beta^{-1} \mathbf{I}_{N_R}) \in \mathbb{C}^{N_{RF} \times 1}$ denote the transmit pilot symbol and noise vector with mean zero and covariance matrix $\beta^{-1} \mathbf{I}_{N_R}$, respectively.

Without loss of generality, we assume $s_{p,k} = 1$ for all p and k , since the pilot sequence is known at the BS and can be readily eliminated [29]. By collecting the received pilot signals from different receive beams corresponding to the p -th transmit beam, the pilot signal $\mathbf{y}_p = [\mathbf{y}_{p,1}^T, \mathbf{y}_{p,2}^T, \dots, \mathbf{y}_{p,K}^T]^T \in \mathbb{C}^{M \times 1}$ with $M = KN_{RF}$ in the p -th subframe can be expressed as

$$\mathbf{y}_p = \mathbf{W}^H \mathbf{H} \mathbf{f}_p + \bar{\mathbf{n}}_p, \quad (6)$$

where $\mathbf{W} = [\mathbf{W}_1^T, \mathbf{W}_2^T, \dots, \mathbf{W}_K^T] \in \mathbb{C}^{N_R \times M}$; $\bar{\mathbf{n}}_p = [(\mathbf{W}_1 \mathbf{n}_{p,1})^T, (\mathbf{W}_2 \mathbf{n}_{p,2})^T, \dots, (\mathbf{W}_K \mathbf{n}_{p,K})^T]^T \in \mathbb{C}^{M \times 1}$ is the equivalent noise vector with covariance matrix

$$\mathbf{R} = \text{blkdiag}(\beta^{-1} \mathbf{W}_1^H \mathbf{W}_1, \dots, \beta^{-1} \mathbf{W}_K^H \mathbf{W}_K). \quad (7)$$

Assuming the utilization of P_0 subframes in the first phase², thus, we have

$$\mathbf{Y}_0 = \mathbf{W}^H \mathbf{H} \mathbf{F} + \bar{\mathbf{N}}, \quad (8)$$

where $\mathbf{F} = [\mathbf{f}_1, \dots, \mathbf{f}_{P_0}] \in \mathbb{C}^{N_T \times P_0}$, $\mathbf{Y}_0 = [\mathbf{y}_1, \dots, \mathbf{y}_{P_0}] \in \mathbb{C}^{M \times P_0}$ and $\bar{\mathbf{N}} = [\bar{\mathbf{n}}_1, \dots, \bar{\mathbf{n}}_{P_0}] \in \mathbb{C}^{M \times P_0}$ are the stacked transmit beam matrix, received pilot matrix and noise matrix, respectively.

Additionally, stacking all transmitted steering vectors and received steering vectors as $\mathbf{A}_T = [\mathbf{a}_T(\psi_1), \dots, \mathbf{a}_T(\psi_L)] \in \mathbb{C}^{N_T \times L}$ and $\mathbf{A}_R = [\mathbf{s}_1 \odot \mathbf{a}_R(\vartheta_1, r_1), \dots, \mathbf{s}_L \odot \mathbf{a}_R(\vartheta_L, r_L)] \in \mathbb{C}^{N_R \times L}$, the channel in (1) can be compactly expressed as

$$\mathbf{H} = \sqrt{N_T N_R} \mathbf{A}_R \mathbf{G} \mathbf{A}_T^H, \quad (9)$$

²We intentionally choose $P_0 \gg L$ to ensure a super-resolution estimation in the first stage.

where $\mathbf{G} = \text{diag}(g_1, \dots, g_L) \in \mathbb{C}^{L \times L}$ is the path gain.

By combining (8) with (9), we have $\mathbf{Y}_0 = \mathbf{C} \mathbf{A}_T^H \mathbf{F} + \bar{\mathbf{N}}$, where $\mathbf{C} = \sqrt{N_T N_R} \mathbf{W}^H \mathbf{A}_R \mathbf{G}$. Define $\mathbf{M} = \mathbf{A}_T \mathbf{C}^H$, the recovery of ψ_l based on \mathbf{Y}_0^H can be formulated as a semidefinite program (SDP) problem [31], i.e.,

$$\begin{aligned} \min_{\mathbf{u}, \mathbf{M}, \mathbf{Z}} \quad & \frac{\mu}{2M} \text{tr}(\mathbf{Z}) + \frac{\mu}{2N_T} \text{tr}(\text{Toep}(\mathbf{u})) \\ & + \frac{1}{2} \|\mathbf{Y}_0^H - \mathbf{F}^H \mathbf{M}\|_F^2 \\ \text{s.t.} \quad & \begin{bmatrix} \text{Toep}(\mathbf{u}) & \mathbf{M} \\ \mathbf{M}^H & \mathbf{Z} \end{bmatrix} \succeq 0, \end{aligned} \quad (10)$$

where μ is a regularization factor, \mathbf{u} and \mathbf{Z} are two auxiliary variables; $\text{Toep}(\mathbf{u})$ is a Toeplitz matrix with \mathbf{u} being its first row. Notably, the problem in (10) is convex and can be directly solved using CVX [32]. The recovery of $\hat{\psi}_l$ is then based on the solution of $\text{Toep}(\mathbf{u})$ by the Multiple Signal Classification (MUSIC) or Estimating Signal Parameter via Rotational Invariance Techniques (ESPRIT) [33], [34].

2) *Stage II: Subchannels Estimation*: Once the AoD parameters are obtained, we can appropriately design the transmit beams in the subsequent subframes to align with the estimated AoDs. In particular, we have $\mathbf{f}_p = \mathbf{a}_T(\hat{\psi}_l)$ for $P_0 + 1 \leq p \leq P$ and $1 \leq l \leq L$ with $P - P_0 \geq L$. In this manner, the received signal in the $(P_0 + l)$ -th subframe can be expressed as

$$\mathbf{y}_{P_0+l} \approx \mathbf{W}^H \mathbf{H} \mathbf{a}_T(\hat{\psi}_l) + \bar{\mathbf{n}}_{P_0+l}. \quad (11)$$

Due to the asymptotic orthogonality of the transmit steering vector, we have $\mathbf{a}_T^H(\psi_l) \mathbf{a}_T(\psi_l) \approx 1$, if $\hat{\psi}_l = \psi_l$, otherwise 0. Therefore, (11) can be rewritten as

$$\mathbf{y}_{P_0+l} \approx \mathbf{W}^H \mathbf{h}_l + \bar{\mathbf{n}}_{P_0+l}, \quad (12)$$

where $\mathbf{h}_l \triangleq \sqrt{N_T N_R} g_l \mathbf{S}_l \mathbf{a}_R(\vartheta_l, r_l)$ is defined as the l -th subchannel with $\mathbf{S}_l = \text{diag}(\mathbf{s}_l)$. For notation simplification, in the subsequent discussion, we simplify \mathbf{y}_{P_0+l} and $\bar{\mathbf{n}}_{P_0+l}$ as \mathbf{y}_l and $\bar{\mathbf{n}}_l$.

In the second stage, our aim is to estimate the subchannel \mathbf{h}_l and extract the corresponding visibility vector \mathbf{s}_l according to the received signal \mathbf{y}_l . To enable efficient estimation, it is crucial to leverage the sparsity of channels. From the perspective of sparsity level, the polar domain emerges as the preferred choice for near-field channels [17]–[19]. However, it necessitates sampling in both the distance and angle domains, resulting in a significantly larger codebook size and increased computational complexity. Consequently, we propose to utilize the angular-domain sparsity as an alternative, as demonstrated in our previous works [7], [28].

Theorem 1. *The angular-domain representation of the $S_n S$ subchannel \mathbf{h}_l is given by*

$$\mathbf{h}_l \approx \mathbf{S}_l \mathbf{D} \mathbf{c}_l, \quad (13)$$

where $\mathbf{c}_l \in \mathbb{C}^{Q \times 1}$ denotes the block-sparse angular channel vector; $\mathbf{D} = [\mathbf{a}(\theta_1), \mathbf{a}(\theta_2), \dots, \mathbf{a}(\theta_Q)] \in \mathbb{C}^{N_R \times Q}$ is angular-domain codebook, where $\{\theta_q : \sin(\theta_q) = \frac{2q-1-Q}{Q}, q \in \mathcal{Q}\}$ and $\mathbf{a}(\theta_q) = 1/\sqrt{N_R} [1, e^{-j\pi \sin(\theta_q)}, \dots, e^{-j\pi(N_R-1) \sin(\theta_q)}]^T$. $Q \geq N_R$ indicates the discrete grid number of angular space and $\mathcal{Q} = \{1, 2, \dots, Q\}$.

Proof: We first consider the inverse Discrete Fourier transformation (IDFT) of \mathbf{h}_l in the angular domain, thus, we have $\mathbf{h}_l = \mathbf{D}\mathbf{c}_l$. Then, utilizing the fact that $s_{l,n} \in \{0, 1\}$, we can easily obtain $\mathbf{h}_l = \mathbf{S}_l \mathbf{h}_l = \mathbf{S}_l \mathbf{D}\mathbf{c}_l$. Therefore, the proof is completed. ■

Remark 1. Notably, through the IDFT operation about \mathbf{h}_l , the SnS property has been implicitly captured in \mathbf{c}_l . However, accurately extracting SnS information directly from \mathbf{c}_l is challenging. An alternative approach is to reconstruct the subchannel $\hat{\mathbf{h}}_l$ based on the estimated $\hat{\mathbf{c}}_l$. Then, SnS information can be obtained using energy detection-based methods [12]. However, these methods depend on the accuracy of the reconstruction of $\hat{\mathbf{h}}_l$ and are sensitive to noise levels. Particularly, in low SNR scenarios, this approach might suffer severe performance degradation. Related simulation results can be found in our previous work [28]. To address this issue, we propose explicitly characterizing SnS characteristics, as shown in (13). This provides an opportunity to directly estimate \mathbf{s}_l .

Utilizing Theorem 1, the received pilot signal in (12) can be rewritten as

$$\mathbf{y}_l \approx \mathbf{W}^H \mathbf{S}_l \mathbf{D}\mathbf{c}_l + \bar{\mathbf{n}}_l, \quad (14)$$

According to (14), the estimation of subchannel \mathbf{h}_l is transformed into the joint estimation of \mathbf{S}_l and \mathbf{c}_l . Since the equivalent noise $\bar{\mathbf{n}}_l$ is colored, we consider to perform a pre-whitening procedure. Assume that the noise covariance matrix \mathbf{R} in (7) can be decomposed by the Cholesky factorization as $\mathbf{R} = \beta^{-1} \mathbf{B}\mathbf{B}^H$, where $\mathbf{B} \in \mathbb{C}^{M \times M}$ is a lower triangular matrix. In this manner, we can obtain the pre-whitening transformation matrix \mathbf{B}^{-1} . Then, the whitened received pilot signal from the l -th path can be rewritten as

$$\tilde{\mathbf{y}}_l = \mathbf{B}^{-1} \mathbf{y}_l \approx \mathbf{P}\mathbf{S}_l \mathbf{D}\mathbf{c}_l + \tilde{\mathbf{n}}_l = \Phi_l \mathbf{c}_l + \tilde{\mathbf{n}}_l, \quad (15)$$

where $\mathbf{P} = \mathbf{B}^{-1} \mathbf{W}^H$, $\tilde{\mathbf{n}}_l = \mathbf{B}^{-1} \bar{\mathbf{n}}_l$ and $\Phi_l = \mathbf{P}\mathbf{S}_l \mathbf{D}$. After whitening, the covariance matrix of the noise $\tilde{\mathbf{n}}_l$ is $\mathbf{B}^{-1} \mathbf{R}\mathbf{B}^{-H} = \beta^{-1} \mathbf{I}_{M \times M}$, thus, $\tilde{\mathbf{n}}_l$ becomes white noise.

The SnS property introduces a dependency between the equivalent measurement matrix Φ_l and \mathbf{S}_l , yet during the channel estimation phase, \mathbf{S}_l remains unknown. While it seems intuitive to estimate Φ_l and \mathbf{c}_l through bilinear inference, establishing a statistical prior model for Φ_l proves challenging due to its dependence on \mathbf{P} , \mathbf{S}_l , and \mathbf{D} . Consequently, existing bilinear inference methods become inapplicable. This highlights the pressing need for novel channel estimation techniques capable of addressing the challenges posed by the SnS property in XL-MIMO systems.

IV. PROPOSED SUBCHANNEL ESTIMATION ALGORITHM

In this section, we formulate the subchannel estimation as a three-layer generalized bilinear inference problem, and propose a computationally effective algorithm based on belief propagation and variational message passing.

A. Probability Model and Factor Graph Representations

To address the potential divergence problem caused by the generic measurement matrix \mathbf{P} , we first perform the unitary

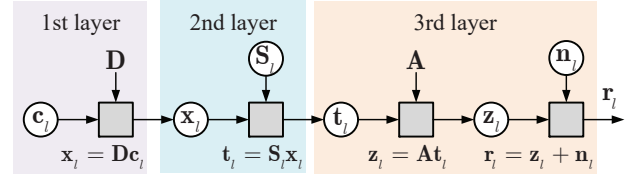


Fig. 3. The three-layer generalized bilinear inference problem is to estimate the angular-domain channel \mathbf{c}_l and visibility indicator matrix \mathbf{S}_l from the received pilot signal \mathbf{y}_l .

TABLE I. Factor and Distribution in (20)

Factor	Distribution	Function
$f_\beta(\beta)$	$p(\beta)$	β^{-1}
$f_{\gamma_l}(\gamma_l)$	$p(\gamma_l)$	$\mathcal{G}a(\gamma_{l,q}; \xi, \eta)$
$f_{\mathbf{c}_l}(\mathbf{c}_l, \gamma_l)$	$p(\mathbf{c}_l \gamma_l)$	(17)
$f_{\mathbf{s}_l}(\mathbf{s}_l)$	$p(\mathbf{s}_l)$	(18)
$f_{\mathbf{x}_l}(\mathbf{x}_l, \mathbf{c}_l)$	$p(\mathbf{x}_l \mathbf{c}_l)$	$\delta(\mathbf{x}_l - \mathbf{D}\mathbf{c}_l)$
$f_{\mathbf{t}_l}(\mathbf{t}_l, \mathbf{s}_l, \mathbf{x}_l)$	$p(\mathbf{t}_l \mathbf{s}_l, \mathbf{x}_l)$	$\delta(\mathbf{t}_l - \mathbf{S}_l \mathbf{x}_l)$
$f_{\mathbf{z}_l}(\mathbf{z}_l, \mathbf{t}_l)$	$p(\mathbf{z}_l \mathbf{t}_l)$	$\delta(\mathbf{z}_l - \mathbf{A}\mathbf{t}_l)$
$f_{\mathbf{r}_l}(\mathbf{r}_l, \mathbf{z}_l, \beta)$	$p(\mathbf{r}_l \mathbf{z}_l, \beta)$	$\mathcal{CN}(\mathbf{r}_l; \mathbf{z}_l, \beta^{-1} \mathbf{I}_M)$

transformation on \mathbf{P} , i.e., $\mathbf{P} = \mathbf{U}\mathbf{A}\mathbf{V}^H$ [35], [36]. Thus, the received pilot signal can be further rewritten as

$$\mathbf{r}_l \approx \mathbf{A}\mathbf{S}_l \mathbf{D}\mathbf{c}_l + \mathbf{n}_l, \quad (16)$$

where $\mathbf{r}_l = \mathbf{U}^H \tilde{\mathbf{y}}_l$, $\mathbf{A} = \mathbf{L}\mathbf{V}^H$, and $\mathbf{n}_l = \mathbf{U}^H \tilde{\mathbf{n}}_l$. Note that, since \mathbf{U} is a unitary matrix, \mathbf{n}_l is still a zero mean Gaussian noise vector with the same covariance matrix as $\tilde{\mathbf{n}}_l$.

The estimation of the SnS channel, as depicted in (16), can be formulated as a three-layer Bayesian inference problem with a single measurement vector (SMV) [37], wherein the simultaneous estimation of the visibility indicator matrix \mathbf{S}_l and the angular channel \mathbf{c}_l is required. More intuitively, we introduce the intermediate variables $\mathbf{x}_l \triangleq \mathbf{D}\mathbf{c}_l$, $\mathbf{t}_l \triangleq \mathbf{S}_l \mathbf{x}_l$, and $\mathbf{z}_l \triangleq \mathbf{A}\mathbf{t}_l$, the three-layer Bayesian inference framework is shown in Fig. 3, where blank circles denote the realizations of the random variables that need to be estimated and gray boxes indicate the function operations. The measurement matrix of the first and third layers \mathbf{D} and \mathbf{A} are known and the second-layer measurement matrix \mathbf{S}_l needs to be estimated.

To capture the angular-domain block sparsity, we assume that the widely used two-layer hierarchical prior for \mathbf{c}_l [38]. Specifically, each element $c_{l,q}$ has a conditionally independent distribution expressed as

$$p(\mathbf{c}_l | \gamma_l) = \prod_{q=1}^Q p(c_{l,q} | \gamma_{l,q}) = \prod_{q=1}^Q \mathcal{CN}(c_{l,q}; 0, \gamma_{l,q}^{-1}), \quad (17)$$

where $\gamma_{l,q} \sim \mathcal{G}a(\gamma_{l,q}; \xi, \eta)$ is modeled as a Gamma prior with ξ and η as the shape parameters to ensure a positive variance. It is evident that $c_{l,q}$ converges to zero as $\gamma_{l,q}^{-1}$ approaches zero, capturing the angular-domain sparsity.

In terms of visibility indicator vector \mathbf{s}_l , since the VR exhibits spatial-correlated property, the non-zero elements of the VR indicator vector \mathbf{s}_l concentrate on a specific subset of the whole array. To capture the spatial correlation, the prior distribution of visibility indicator vector \mathbf{s}_l can be characterized with a one-order Markov chain as

$$p(\mathbf{s}_l) = \prod_{n=1}^N p(s_{l,n} | s_{l,n-1}), \quad (18)$$

$$\begin{aligned}
& p(\gamma_l, \mathbf{c}_l, \mathbf{x}_l, \mathbf{s}_l, \mathbf{t}_l, \mathbf{z}_l, \beta | \mathbf{r}_l) \propto p(\mathbf{r}_l | \mathbf{z}_l, \beta) p(\beta) p(\mathbf{z}_l | \mathbf{t}_l) p(\mathbf{t}_l | \mathbf{s}_l, \mathbf{x}_l) p(\mathbf{s}_l) p(\mathbf{x}_l | \mathbf{c}_l) p(\mathbf{c}_l | \gamma_l) p(\gamma_l) \\
& \triangleq \underbrace{f_{\mathbf{x}_l}(\mathbf{x}_l, \mathbf{c}_l) f_{\mathbf{c}_l}(\mathbf{c}_l, \gamma_l) f_{\gamma_l}(\gamma_l)}_{\text{the first layer}} \underbrace{f_{\mathbf{t}_l}(\mathbf{t}_l, \mathbf{s}_l, \mathbf{x}_l) f_{\mathbf{s}_l}(\mathbf{s}_l)}_{\text{the second layer}} \underbrace{f_{\mathbf{r}_l}(\mathbf{r}_l, \mathbf{z}_l, \beta) f_{\mathbf{z}_l}(\mathbf{z}_l, \mathbf{t}_l) f_{\beta}(\beta)}_{\text{the third layer}}
\end{aligned} \tag{20}$$

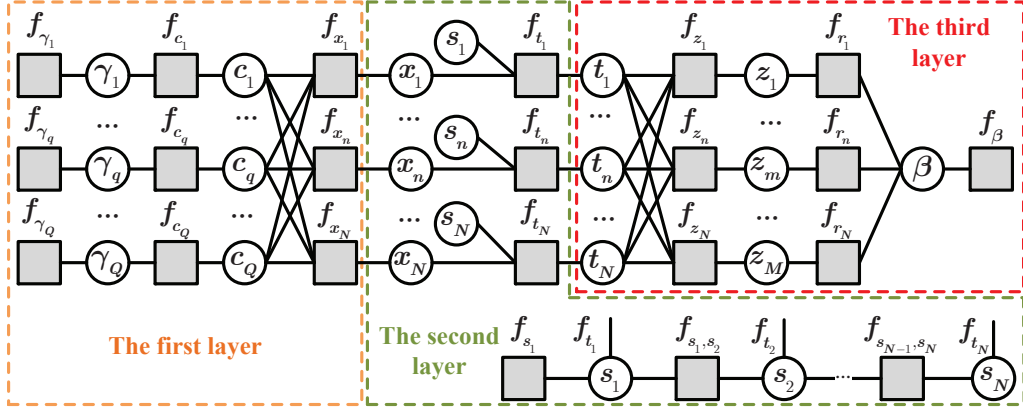


Fig. 4. Illustration of factor graph representations of (20).

where $p(s_{l,n} | s_{l,n-1}) = (1 - \phi_l) \delta(1 - s_{l,n}) + \phi_l \delta(s_{l,n})$, where ϕ_l reflects the sparsity level of SnS channels. The transition probability of Markov chain is given by

$$p(s_{l,n} | s_{l,n-1}) = \begin{cases} (1 - p_{01})^{1-s_{l,n}} p_{01}^{s_{l,n}}, & s_{l,n-1} = 0, \\ p_{10}^{1-s_{l,n}} (1 - p_{10})^{s_{l,n}}, & s_{l,n-1} = 1, \end{cases} \tag{19}$$

where $p_{01} = p(s_{l,n} = 0 | s_{l,n-1} = 1)$ and other three transition probabilities are defined similarly. By the steady-state assumption, the Markov chain can be completely characterized by two parameters ϕ_l and p_{10} . The other three transition probabilities can be easily obtained as $p_{01} = \phi_l p_{10} / (1 - \phi_l)$, $p_{00} = 1 - p_{01}$, and $p_{11} = 1 - p_{10}$, respectively.

Based on the prior distribution of \mathbf{c}_l and \mathbf{s}_l provided in (17) and (18), the joint posterior distribution of γ_l , \mathbf{c}_l , \mathbf{x}_l , \mathbf{s}_l , \mathbf{t}_l , \mathbf{z}_l , and β given \mathbf{r}_l can be factorized as (20), as shown in the top of this page, where the involved probability distributions are listed in Table I. For brevity, we omit the subscript l in the subsequent derivation. Moreover, the factor graph representation of (20) is depicted in Fig. 4, where the gray squares represent the factor nodes, and the blank circles represent the variable nodes.

Based on the probabilistic model provided in (20), the optimal estimators of \mathbf{s} and \mathbf{c} under the minimum mean square error (MMSE) principle can be derived as

$$\hat{\mathbf{s}}_n = \int \mathbf{s}_n p(\mathbf{s}_n | \mathbf{r}) d\mathbf{s}_n, \forall n \in \mathcal{N}, \tag{21}$$

$$\hat{\mathbf{c}}_q = \int \mathbf{c}_q p(\mathbf{c}_q | \mathbf{r}) d\mathbf{c}_q, \forall q \in \mathcal{Q}, \tag{22}$$

where the posterior probabilistic distribution $p(\mathbf{s}_n | \mathbf{r})$ and $p(\mathbf{c}_q | \mathbf{r})$ are respectively given by

$$p(\mathbf{s}_n | \mathbf{r}) = \int p(\gamma, \mathbf{c}, \mathbf{x}, \mathbf{s}, \mathbf{t}, \mathbf{z}, \beta | \mathbf{r}) d\gamma d\mathbf{c} d\mathbf{x} d\mathbf{t} d\mathbf{z} d\beta d\mathbf{s}_{\setminus n}, \tag{23}$$

$$p(\mathbf{c}_q | \mathbf{r}) = \int p(\gamma, \mathbf{c}, \mathbf{x}, \mathbf{s}, \mathbf{t}, \mathbf{z}, \beta | \mathbf{r}) d\gamma d\mathbf{s} d\mathbf{t} d\mathbf{z} d\beta d\mathbf{c}_{\setminus q}, \tag{24}$$

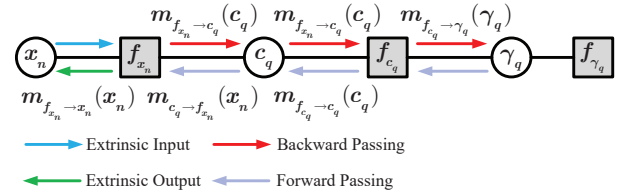


Fig. 5. Illustration of message passing in the first layer.

with $\mathbf{s}_{\setminus n}$ and $\mathbf{c}_{\setminus q}$ denotes the all elements of \mathbf{s} and \mathbf{c} except s_n and c_q , respectively.

Given the substantial number of antenna elements in XL-MIMO systems, both MMSE estimators (21) and (22) involve high-dimensional integrals, making them impractical to compute. Recently, low-complexity techniques such as GAMP [37]–[41] have been extensively employed for solving the maximum a posteriori (MAP) estimation problem. For instance, building on the GAMP method [39], [40], the work in [41] introduced a novel bilinear message-scheduling GAMP method, which jointly addresses device activity detection, channel estimation, and data decoding in a grant-free massive MIMO scenario. Furthermore, in [37], the bilinear GAMP approach was extended to the multi-layer case to handle cascaded problems in relay communication systems. Motivated by the success of the multi-layer bilinear GAMP in cascaded estimation problems, we propose a computationally efficient three-layer GAMP algorithm to solve the MMSE estimation problem in (21) and (22). In the following, we will elaborate on the details of message passing in each layer.

B. Message Passing in the First Layer

In the first layer, the sparsity of angular channel \mathbf{c} is captured, and corresponding coefficients c_q , $\forall q \in \mathcal{Q}$ are estimated by exploiting the prior distribution information and the likelihood messages from the second layer. Meanwhile, the prior distribution information associated with \mathbf{x} is output for the second layer. Fig. 5 illustrates the message passing in the first layer.

Denote the message from x_n to f_{x_n} and the belief of c_q as $m_{x_n \rightarrow f_{x_n}}(x_n) \propto \mathcal{CN}(x_n; \vec{x}_n, \vec{v}_n^x)$ and $b(c_q) \propto \mathcal{CN}(c_q; \hat{c}_q, \hat{v}_q^c)$, respectively. Based on the variational message passing rule [36], [38], the message from f_{c_q} to γ_q can be derived as

$$m_{f_{c_q} \rightarrow \gamma_q}(\gamma_q) \propto \exp \left\{ \int \log f_{c_q}(c_q, \gamma_q) b(c_q) dc_q \right\} \quad (25)$$

$$\propto \gamma_q \exp \left\{ -\gamma_q \left(|\hat{c}_q|^2 + \hat{v}_q^c \right) \right\}.$$

Combining the likelihood message $m_{f_{c_q} \rightarrow \gamma_q}(\gamma_q)$ in (25) and the prior message $f_{\gamma_q}(\gamma_q)$ associated with γ_q , the belief of γ_q is denoted as

$$b(\gamma_q) \propto m_{f_{c_q} \rightarrow \gamma_q}(\gamma_q) f_{\gamma_q}(\gamma_q)$$

$$= \gamma_q^\xi \exp \left\{ -\gamma_q \left(\eta + |\hat{c}_q|^2 + \hat{v}_q^c \right) \right\}. \quad (26)$$

From (26), it can be seen that $b(\gamma_q)$ obeys the Gamma distribution with the shape parameters $\xi + 1$ and $\eta + |\hat{c}_q|^2 + \hat{v}_q^c$. Hence, the approximate posterior mean of γ_q is given by

$$\hat{\gamma}_q = \frac{\xi + 1}{\eta + |\hat{c}_q|^2 + \hat{v}_q^c}. \quad (27)$$

With the belief γ_q and variational message passing rule, the message from f_{c_q} to c_q is given by

$$m_{f_{c_q} \rightarrow c_q}(c_q) \propto \exp \left\{ \int \log f_{c_q}(c_q, \gamma_q) b(\gamma_q) d\gamma_q \right\} \quad (28)$$

$$= \mathcal{CN}(c_q; 0, \hat{\gamma}_q^{-1}).$$

Combining $m_{f_{c_q} \rightarrow c_q}(c_q)$ in (28) and the message $m_{c_q \rightarrow f_{c_q}}(c_q)$ derived in (39), the belief of c_q is given by

$$b(c_q) \propto m_{c_q \rightarrow f_{c_q}}(c_q) m_{f_{c_q} \rightarrow c_q}(c_q) = \mathcal{CN}(c_q; \hat{c}_q, \hat{v}_q^c), \quad (29)$$

where \hat{v}_q^c and \hat{c}_q are respectively given by

$$\hat{v}_q^c = (1/\bar{v}_q^c + \hat{\gamma}_q)^{-1}, \quad \hat{c}_q = \bar{c}_q / (1 + \hat{\gamma}_q \bar{v}_q^c). \quad (30)$$

Denote the message from f_{x_n} to c_q as $m_{f_{x_n} \rightarrow c_q}(c_q) \propto \mathcal{CN}(c_q; \vec{c}_{n,q}, \vec{v}_{n,q}^c)$ derived in (36). According to the belief propagation rule [42], the message from c_q to f_{x_n} can be derived as

$$m_{c_q \rightarrow f_{x_n}}(c_q) \propto \frac{b(c_q)}{m_{f_{x_n} \rightarrow c_q}(c_q)} = \mathcal{CN}(c_q; \vec{c}_{q,n}, \vec{v}_{q,n}^c), \quad (31)$$

where $\vec{v}_{q,n}^c$ and $\vec{c}_{q,n}$ are respectively given by

$$\vec{v}_{q,n}^c = (1/\hat{c}_q - 1/\vec{c}_{n,q})^{-1}, \quad (32)$$

$$\vec{c}_{q,n} = \vec{v}_{q,n}^c (\hat{c}_q / \hat{v}_q^c - \vec{c}_{n,q} / \vec{v}_{n,q}^c). \quad (33)$$

Given the message $m_{c_q \rightarrow f_{x_n}}(x_n)$ in (31), the message $m_{f_{x_n} \rightarrow x_n}(x_n)$ of the first layer from f_{x_n} to x_n is given by

$$m_{f_{x_n} \rightarrow x_n}(x_n) \propto \int f_{x_n}(x_n, \mathbf{c}) \prod_{q=1}^Q m_{c_q \rightarrow f_{x_n}}(c_q) dc \quad (34)$$

$$= \mathcal{CN}(x_n; \vec{x}_n, \vec{v}_n^x),$$

where $\mathbf{d}_n \in \mathbb{C}^Q$ denotes the n -th row of \mathbf{D} ; \vec{x}_n and \vec{v}_n^x are respectively calculated as

$$\vec{x}_n = \sum_{q=1}^Q d_{n,q} \vec{c}_{q,n}, \quad \vec{v}_n^x = \sum_{q=1}^Q |d_{n,q}|^2 \vec{v}_{q,n}^c. \quad (35)$$

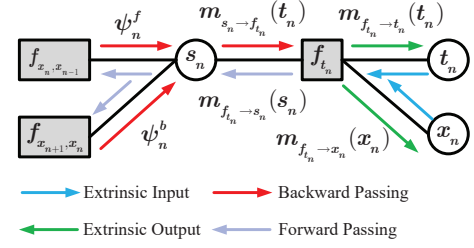


Fig. 6. Illustration of message passing in the second layer.

Combining the messages $m_{x_n \rightarrow f_{x_n}}(x_n)$ from the second layer and $m_{c_i \rightarrow f_{x_n}}(c_i)$ with $i \neq q$, the message from f_{x_n} to c_q can be given by

$$m_{f_{x_n} \rightarrow c_q}(c_q) \propto \int f_{x_n}(x_n, \mathbf{c}) m_{x_n \rightarrow f_{x_n}}(x_n)$$

$$\prod_{i \neq q}^Q m_{c_i \rightarrow f_{x_n}}(c_i) dc_{\setminus q} dx_n \quad (36)$$

$$= \mathcal{CN}(c_m; \vec{c}_{n,q}, \vec{v}_{n,q}^c),$$

where the $\vec{c}_{n,q}$ and $\vec{v}_{n,q}^c$ are respectively given by

$$\vec{c}_{n,q} = \frac{\vec{x}_n - \sum_{i \neq q}^Q d_{n,i} \vec{c}_{i,n}}{d_{n,q}} = \frac{\vec{x}_n - \vec{x}_n + d_{n,q} \vec{c}_{q,n}}{d_{n,q}}, \quad (37)$$

$$\vec{v}_{n,q}^c = \frac{\vec{v}_n^x + \sum_{i \neq q}^Q |d_{n,i}|^2 \vec{v}_{i,n}^c}{|d_{n,q}|^2} = \frac{\vec{v}_n^x + \vec{v}_n^x - |d_{n,q}|^2 \vec{v}_{q,n}^c}{|d_{n,q}|^2}. \quad (38)$$

Then, the message from c_q to f_{c_q} is calculated as

$$m_{c_q \rightarrow f_{c_q}}(c_q) \propto \prod_{n=1}^{N_R} m_{f_{x_n} \rightarrow c_q}(c_q) = \mathcal{CN}(c_q; \vec{c}_q, \vec{v}_q^c), \quad (39)$$

where the variance \vec{v}_q^c and mean \vec{c}_q are respectively defined as

$$\vec{v}_q^c = \left(\sum_{n=1}^{N_R} (1/\vec{v}_{n,q}^c) \right)^{-1}, \quad \vec{c}_q = \vec{v}_q^c \sum_{n=1}^{N_R} (\vec{c}_{n,q} / \vec{v}_{n,q}^c). \quad (40)$$

C. Message Passing in the Second Layer

In the second layer, the SnS property is captured, and the visibility indicator vector s_n for $n = 1, 2, \dots, N_R$ are estimated by exploiting the messages from the first and third layers. Meanwhile, the likelihood and prior information associated with x_n and t_n for the first and third layers are output. The message passing is shown in Fig. 6, where $f_{x_n, x_{n-1}} \triangleq p(s_n | s_{n-1})$.

Denote the message from the third layer as $m_{t_n \rightarrow f_{t_n}}(t_n) \propto \mathcal{CN}(t_n; \vec{t}_n, \vec{v}_n^t)$ derived in (65). Thus, the message from f_{t_n} to s_n can be given by (41), as shown in the top of next page, where (a) is obtained according to the fact $\int \delta(x) f(x) dx = f(0)$ and $s_n \in \{0, 1\}$. In addition, π_n^{out} is defined as

$$\pi_n^{\text{out}} = \frac{\mathcal{CN}(0; \vec{t}_n + \vec{x}_n, \vec{v}_n^t + \vec{v}_n^x)}{\mathcal{CN}(0; \vec{t}_n, \vec{v}_n^t) + \mathcal{CN}(0; \vec{t}_n + \vec{x}_n, \vec{v}_n^t + \vec{v}_n^x)}. \quad (42)$$

With the message $m_{f_{t_n} \rightarrow s_n}(s_n)$ in (41), the message from s_n to f_{t_n} is given by

$$m_{s_n \rightarrow f_{t_n}}(s_n) \propto (1 - \pi_n^{\text{in}}) \delta(s_n) + \pi_n^{\text{in}} \delta(1 - s_n), \quad (43)$$

$$\begin{aligned}
m_{f_{t_n} \rightarrow s_n}(s_n) &\propto \int f_{t_n}(t_n, s_n, x_n) m_{t_n \rightarrow f_{t_n}}(t_n) m_{x_n \rightarrow f_{x_n}}(x_n) dx_n dt_n \\
&= \mathcal{CN}(0; \vec{t}_n, \vec{v}_n^t) \delta(s_n) + \mathcal{CN}(0; \vec{t}_n + \vec{x}_n, \vec{v}_n^t + \vec{v}_n^x) \delta(1 - s_n) \\
&\stackrel{(a)}{\propto} (1 - \pi_n^{\text{out}}) \delta(s_n) + \pi_n^{\text{out}} \delta(1 - s_n),
\end{aligned} \tag{41}$$

where π_n^{in} is defined as

$$\pi_n^{\text{in}} = \frac{\psi_n^f \psi_n^b}{\psi_n^f \psi_n^b + (1 - \psi_n^f)(1 - \psi_n^b)}. \tag{44}$$

Here, ψ_n^f and ψ_n^b are the forward and backward messages along the Markov chain, and are respectively defined as [28]

$$\psi_n^f = \frac{p_{01}(1 - \psi_{n-1}^f)(1 - \pi_{n-1}^{\text{out}}) + p_{11}\lambda_{n-1}^f \pi_{n-1}^{\text{out}}}{(1 - \psi_{n-1}^f)(1 - \pi_{n-1}^{\text{out}}) + \psi_{n-1}^f \pi_{n-1}^{\text{out}}}, \tag{45}$$

$$\psi_n^b = \frac{p_{10}(1 - \psi_{n+1}^b)(1 - \pi_{n+1}^{\text{out}}) + p_{11}\psi_{n+1}^b \pi_{n+1}^{\text{out}}}{p_{01}(1 - \psi_{n+1}^b)(1 - \pi_{n+1}^{\text{out}}) + p_{11}\psi_{n+1}^b \pi_{n+1}^{\text{out}}}. \tag{46}$$

where $p_0 = p_{10} + p_{00}$, $p_1 = p_{11} + p_{01}$.

Combining the message $m_{f_{t_n} \rightarrow s_n}(s_n)$ in (42) and $m_{s_n \rightarrow f_{t_n}}(s_n)$ in (44), the belief of s_n can be given by

$$b(s_n) = \frac{\psi_n^f \psi_n^b \pi_n^{\text{out}}}{\psi_n^f \psi_n^b \pi_n^{\text{out}} + (1 - \psi_n^f)(1 - \psi_n^b)(1 - \pi_n^{\text{out}})}, \tag{47}$$

which indicates the visibility probability of the n -th antenna. If $b(s_n)$ is greater than a threshold, the n -th antenna is regarded as being visible, i.e.,

$$\hat{s}_n = \begin{cases} 1, & b(s_n) > \psi_{\text{th}}, \\ 0, & b(s_n) \leq \psi_{\text{th}}, \end{cases} \tag{48}$$

where ψ_{th} is a predetermined threshold. Using the obtained $b(s_n)$, ψ_0^f in (45) and is updated in each iteration as [43]

$$\psi_0^f = \frac{1}{N_R} \sum_{n=1}^{N_R} b(s_n). \tag{49}$$

With the message $m_{s_n \rightarrow f_{t_n}}(s_n)$ in (43) and $m_{t_n \rightarrow f_{t_n}}(t_n)$ in (65), the output message $m_{f_{t_n} \rightarrow x_n}(x_n)$ from f_{t_n} to x_n is given by

$$\begin{aligned}
m_{f_{t_n} \rightarrow x_n}(x_n) &\propto \int f_{t_n}(t_n, s_n, x_n) m_{s_n \rightarrow f_{t_n}}(s_n) \\
&\quad m_{t_n \rightarrow f_{t_n}}(t_n) ds_n dt_n \\
&\propto \mathcal{CN}(x_n; \vec{t}_n, \vec{v}_n^t).
\end{aligned} \tag{50}$$

Furthermore, since x_n is only connected with f_{t_n} and f_{x_n} in the factor graphs, the message from x_n to f_{x_n} also satisfies $m_{x_n \rightarrow f_{x_n}}(x_n) \propto \mathcal{CN}(x_n; \vec{t}_n, \vec{v}_n^t)$. Thus, we have $\vec{x}_n = \vec{t}_n$ and $\vec{v}_n^x = \vec{v}_n^t$. Similarly, the output message $m_{f_{t_n} \rightarrow t_n}(t_n)$ from f_{t_n} to t_n is given by

$$m_{f_{t_n} \rightarrow t_n}(t_n) = (1 - \pi_n^{\text{in}}) \delta(t_n) + \pi_n^{\text{in}} \mathcal{CN}(t_n; \vec{x}_n, \vec{v}_n^x). \tag{51}$$

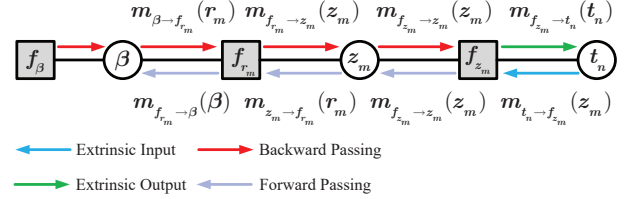


Fig. 7. Illustration message passing in the third layer.

D. Message Passing in the Third Layer

In the third layer, the variables t_n , $\forall n \in \mathcal{N}$, are decoupled from \mathbf{r} and estimated by combining the messages from the second layer. Meanwhile, the likelihood information associated with t_n is output for the second layer. The message passing is shown in Fig. 7.

Denote the message from f_{z_m} to t_n and the belief of t_n as $m_{f_{z_m} \rightarrow t_n} \propto \mathcal{CN}(t_n; \vec{t}_{n,m}, \vec{v}_{n,m}^t)$ and $b(t_n) \sim \mathcal{CN}(t_n; \hat{t}_n, \hat{v}_n^t)$, respectively. According to the belief propagation rule, the message from t_n to f_{z_m} can be given by

$$m_{t_n \rightarrow f_{z_m}}(t_n) \propto \frac{b(t_n)}{m_{f_{z_m} \rightarrow t_n}(t_n)} = \mathcal{CN}(t_n; \vec{t}_{n,m}, \vec{v}_{n,m}^t), \tag{52}$$

where $\vec{v}_{n,m}^t$ and $\vec{t}_{n,m}$ are respectively given by

$$\vec{v}_{n,m}^t = 1 / (1/\hat{v}_n^t - 1/\vec{v}_{m,n}^t), \tag{53}$$

$$\vec{t}_{n,m} = \vec{v}_{n,m}^t (\hat{t}_n/\hat{v}_n^t - \vec{t}_{m,n}/\vec{v}_{m,n}^t). \tag{54}$$

With the message $m_{t_n \rightarrow f_{z_m}}(t_n)$, the message from f_{z_m} to z_m is given by

$$\begin{aligned}
m_{f_{z_m} \rightarrow z_m}(z_m) &= \int f_{z_m}(z_m, \mathbf{t}) \prod_{n=1}^{N_R} m_{t_n \rightarrow f_{z_m}}(t_n) dt \\
&\propto \mathcal{CN}(z_m; \vec{z}_m, \vec{v}_m^z).
\end{aligned} \tag{55}$$

where $\mathbf{a}_m \in \mathbb{C}^N$ denotes the m -th row of \mathbf{A} ; \vec{z}_m and \vec{v}_m^z are respectively calculated as

$$\vec{z}_m = \sum_{n=1}^{N_R} a_{m,n} \vec{t}_{n,m}, \quad \vec{v}_m^z = \sum_{n=1}^{N_R} |a_{m,n}|^2 \vec{v}_{n,m}^t. \tag{56}$$

Denote the belief of z_m as $b(z_m) \propto \mathcal{CN}(z_m; \hat{z}_m, \hat{v}_m^z)$ provided in (61). Similar to (25), the message from f_{r_m} to β is given by

$$\begin{aligned}
m_{f_{r_m} \rightarrow \beta}(\beta) &\propto \exp \left\{ \int \log f_{r_m}(r_m, \beta) b(z_m) dz_m \right\} \\
&\propto \beta \exp \left\{ -\beta \left(|r_m - \hat{z}_m|^2 + \hat{v}_m^z \right) \right\}.
\end{aligned} \tag{57}$$

Combining the prior message $f_\beta(\beta)$ and $m_{f_{r_m} \rightarrow \beta}(\beta)$ in (57), the belief of β is given by

$$b(\beta) \propto \beta^{M-1} \exp \left\{ -\beta \sum_{m=1}^M \left(|r_m - \hat{z}_m|^2 + \hat{v}_m^z \right) \right\}. \tag{58}$$

It is observed that the belief $b(\beta)$ obeys the Gamma distribution with shape parameters M and $\sum_{m=1}^M (|r_m - \hat{z}_m|^2 + \hat{\nu}_m^z)$. Thus, the approximate posterior mean $\hat{\beta}$ is given by

$$\hat{\beta} = \frac{M}{\sum_{m=1}^M (|r_m - \hat{z}_m|^2 + \hat{\nu}_m^z)}. \quad (59)$$

With $b(\beta)$, the message from f_{r_m} to z_m is given by

$$m_{f_{r_m} \rightarrow z_m}(z_m) \propto \exp \left\{ \int \log f_{r_m}(r_m, \beta) b(\beta) d\beta \right\} \quad (60)$$

$$\propto \mathcal{CN}(z_m; r_m, \hat{\beta}^{-1}).$$

Furthermore, since z_m is only connected with f_{r_m} and f_{z_m} in the factor graph, the message from z_m to f_{z_m} is given by $m_{z_m \rightarrow f_{z_m}}(z_m) \propto \mathcal{CN}(z_m; r_m, \hat{\beta}^{-1})$.

Combining $m_{z_m \rightarrow f_{z_m}}(z_m)$ and $m_{f_{z_m} \rightarrow z_m}(z_m)$ in (60) and (55), the belief of z_m is given by

$$b(z_m) \propto \mathcal{CN}(z_m; \hat{z}_m, \hat{\nu}_m^z), \quad (61)$$

where $\hat{\nu}_m^z$ and \hat{z}_m are respectively given by

$$\hat{\nu}_m^z = \left(\hat{\beta} + 1/\bar{\nu}_m^z \right)^{-1}, \quad \hat{z}_m = \hat{\nu}_m^z \left(r_m \hat{\beta} + \bar{z}_m / \bar{\nu}_m^z \right). \quad (62)$$

With the messages $m_{z_m \rightarrow f_{z_m}}(z_m)$ and $m_{t_i \rightarrow f_{z_m}}(t_i)$ with $i \neq n$, the message from f_{z_m} to t_n is given by

$$m_{f_{z_m} \rightarrow t_n}(t_n) = \int f_{z_m}(z_m, \mathbf{t}) m_{z_m \rightarrow f_{z_m}}(z_m) \quad (63)$$

$$\prod_{\substack{i=1 \\ i \neq n}}^{N_R} m_{t_i \rightarrow f_{z_m}}(t_i) dz_m dt_{\setminus n}$$

$$\propto \mathcal{CN}(t_n, \vec{t}_{m,n}, \vec{\nu}_{m,n}^t),$$

where $\vec{t}_{m,n}$ and $\vec{\nu}_{m,n}^t$ are respectively given by

$$\vec{t}_{m,n} = \frac{r_m - \bar{z}_m}{a_{m,n}} + \vec{t}_{n,m}, \quad (64)$$

$$\vec{\nu}_{m,n}^t = \frac{\hat{\beta}^{-1} + \bar{\nu}_m^z - |a_{m,n}|^2 \bar{\nu}_{n,m}^t}{|a_{m,n}|^2}.$$

Combining the message $m_{f_{z_m} \rightarrow t_n}(t_n)$ for all m , the output message $m_{f_{t_n} \rightarrow t_n}(t_n)$ from t_n to f_{t_n} is given by

$$m_{t_n \rightarrow f_{t_n}}(t_n) = \prod_{m=1}^M m_{f_{z_m} \rightarrow t_n}(t_n) \propto \mathcal{CN}(t_n; \vec{t}_n, \vec{\nu}_n^t), \quad (65)$$

where the variance \vec{t}_n and mean $\vec{\nu}_n^t$ are respectively given by

$$\vec{\nu}_n^t = \left(\sum_{m=1}^M (1/\bar{\nu}_{m,n}^t) \right)^{-1}, \quad \vec{t}_n = \vec{\nu}_n^t \sum_{m=1}^M (\vec{t}_{m,n}/\bar{\nu}_{m,n}^t). \quad (66)$$

With $m_{f_{t_n} \rightarrow t_n}(t_n)$ and $m_{t_n \rightarrow f_{t_n}}(t_n)$, we have $b(t_n) \propto ((1 - \pi_n^{\text{in}})\delta(t_n) + \pi_n^{\text{in}}\mathcal{CN}(t_n; \vec{x}_n, \vec{\nu}_n^x))\mathcal{CN}(t_n; \vec{t}_n, \vec{\nu}_n^t)$. Thus, the approximate posterior probability distribution of t_n is given by (67), as shown in the top of next page, where the auxiliary variables S_n , w_n , ν_n^{tmp} , and t_n^{tmp} are respectively given by $S_n = \mathcal{CN}(0; \vec{t}_n - \vec{x}_n, \vec{\nu}_n^t + \vec{\nu}_n^x)$, $\omega_n = \pi_n^{\text{in}} S_n / ((1 - \pi_n^{\text{in}})\mathcal{CN}(0; \vec{t}_n, \vec{\nu}_n^t) + \pi_n^{\text{in}} S_n)$, $\nu_n^{\text{tmp}} = (1/\vec{\nu}_n^t + 1/\vec{\nu}_n^x)^{-1}$, and $t_n^{\text{tmp}} = \nu_n^{\text{tmp}} (\vec{t}_n/\vec{\nu}_n^t + \vec{x}_n/\vec{\nu}_n^x)$.

According to (67), the posterior mean \hat{t}_n and variance $\hat{\nu}_n^t$ are respectively given by

$$\hat{t}_n = \int t_n p(t_n | \mathbf{r}) dt_n = \omega_n t_n^{\text{tmp}} \quad (68)$$

$$\hat{\nu}_n^t = \int |t_n - \hat{t}_n|^2 p(t_n | \mathbf{r}) dt_n \quad (69)$$

$$= \omega_n \left((1 - \omega_n) |\hat{t}_n|^2 + \nu_n^{\text{tmp}} \right).$$

Note that due to the fact that \mathbf{t} is equal to \mathbf{SDc} , the posterior mean $\hat{\mathbf{t}}$ can be equivalently seen as the approximate posterior estimation of SnS subchannel \mathbf{h} .

E. Messages Approximation in Factor Nodes f_{z_m} and f_{x_n}

From the factor graphs shown in Fig. 4, it is clear that there are MN edges between f_{z_m} and t_n for all m and n . Similarly, there are NQ edges between f_{x_n} and c_q for all n and q . Therefore, $2MN + 2NQ$ messages have to be updated for forward and backward message passing in each iteration. To further reduce the computational complexity of message passing, we can approximate the means and variances of Gaussian messages by omitting some small terms.

1) *Messages approximation for $m_{t_n \rightarrow f_{z_m}}(t_n)$ and $m_{c_q \rightarrow f_{x_n}}(c_q)$* : According to (66), it can be seen that $\vec{\nu}_n^t \ll \bar{\nu}_{m,n}^t$ when N is large enough. Meanwhile, according to the Bayesian theory, we have $\hat{\nu}_n^t < \bar{\nu}_{m,n}^t$ [38]. Thus, the variance $\bar{\nu}_{n,m}^t = 1/(1/\hat{\nu}_n^t - 1/\bar{\nu}_{m,n}^t) \approx \hat{\nu}_n^t$. Utilizing (64) and $\bar{\nu}_{n,m}^t \approx \hat{\nu}_n^t$, the mean $\vec{t}_{n,m}$ can be approximated as

$$\vec{t}_{n,m} \approx \hat{\nu}_n^t \left(\frac{\hat{t}_n}{\hat{\nu}_n^t} - \frac{a_{m,n}^* (r_m - \bar{z}_m + a_{m,n} \vec{t}_{n,m})}{\hat{\beta}^{-1} + \bar{\nu}_m^z - |a_{m,n}|^2 \bar{\nu}_{n,m}^t} \right) \quad (70)$$

$$\stackrel{(a)}{\approx} \hat{t}_n - a_{m,n}^* \hat{\nu}_n^t \frac{r_m - \bar{z}_m}{\hat{\beta}^{-1} + \bar{\nu}_m^z},$$

where (a) is obtained utilizing the fact that $\bar{z}_m \gg a_{m,n} \vec{t}_{n,m}$ and $\bar{\nu}_m^z \gg |a_{m,n}|^2 \bar{\nu}_{n,m}^t$ from (56). Similarly, the variance $\bar{\nu}_{q,n}^c$ and mean $\vec{c}_{q,n}$ provided in (32) can be approximated as

$$\bar{\nu}_{q,n}^c = 1/(1/\hat{\nu}_q^c - 1/\bar{\nu}_{n,q}^c) \approx \hat{c}_q, \quad (71)$$

$$\vec{c}_{q,n} \approx \hat{c}_q - d_{n,q}^* \hat{\nu}_q^c \frac{\vec{x}_n - \bar{x}_n}{\bar{\nu}_n^x + \bar{\nu}_n^c}. \quad (72)$$

2) *Messages approximation for $m_{f_{z_m} \rightarrow z_m}(z_m)$ and $m_{f_{x_n} \rightarrow x_n}(x_n)$* : With the approximated $\bar{\nu}_{n,m}^t$ and $\vec{t}_{n,m}$, the variance $\bar{\nu}_m^z$ and mean \bar{z}_m provided in (56) can be simplified as

$$\bar{\nu}_m^z = \sum_{n=1}^{N_R} |a_{m,n}|^2 \bar{\nu}_{n,m}^t \approx \sum_{n=1}^{N_R} |a_{m,n}|^2 \hat{\nu}_n^t, \quad (73)$$

$$\bar{z}_m = \sum_{n=1}^{N_R} a_{m,n} \vec{t}_{n,m} \approx \sum_{n=1}^{N_R} a_{m,n} \hat{t}_n - \bar{\nu}_m^z \frac{r_m - \bar{z}_m}{\hat{\beta}^{-1} + \bar{\nu}_m^z}. \quad (74)$$

Similarly, the variance $\bar{\nu}_n^x$ and mean \bar{x}_n can be also approximated as

$$\bar{\nu}_n^x = \sum_{q=1}^Q |d_{n,q}|^2 \bar{\nu}_{q,n}^c \approx \sum_{q=1}^Q |d_{n,q}|^2 \hat{\nu}_q^c, \quad (75)$$

$$\bar{x}_n = \sum_{q=1}^Q d_{n,q} \vec{c}_{q,n} \approx \sum_{q=1}^Q d_{n,q} \hat{c}_q - \bar{\nu}_n^x \frac{\vec{x}_n - \bar{x}_n}{\bar{\nu}_n^x + \bar{\nu}_n^c}. \quad (76)$$

$$\begin{aligned}
p(t_n|\mathbf{r}) &= \frac{((1 - \pi_n^{\text{in}})\delta(t_n) + \pi_n^{\text{in}}\mathcal{CN}(t_n; \bar{x}_n, \bar{v}_n^x)) \mathcal{CN}(t_n; \bar{t}_n, \bar{v}_n^t)}{\int ((1 - \pi_n^{\text{in}})\delta(t_n) + \pi_n^{\text{in}}\mathcal{CN}(t_n; \bar{x}_n, \bar{v}_n^x)) \mathcal{CN}(t_n; \bar{t}_n, \bar{v}_n^t) dt_n} \\
&= \frac{(1 - \pi_n^{\text{in}})\mathcal{CN}(t_n; \bar{t}_n, \bar{v}_n^t)\delta(t_n) + \pi_n^{\text{in}}\mathcal{CN}(t_n; \bar{x}_n, \bar{v}_n^x)\mathcal{CN}(t_n; \bar{t}_n, \bar{v}_n^t)}{(1 - \pi_n^{\text{in}})\mathcal{CN}(0; \bar{t}_n, \bar{v}_n^t) + \pi_n^{\text{in}} \int \mathcal{CN}(t_n; \bar{x}_n, \bar{v}_n^x)\mathcal{CN}(t_n; \bar{t}_n, \bar{v}_n^t) dt_n} \\
&= (1 - \omega_n)\delta(t_n) + \omega_n\mathcal{CN}(t_n; t_n^{\text{tmp}}, \nu_n^{\text{tmp}}),
\end{aligned} \tag{67}$$

3) Messages approximation for $m_{t_n \rightarrow f_{t_n}}(t_n)$ and $m_{c_q \rightarrow f_{c_q}}(c_q)$:

$$\bar{v}_n^t \stackrel{(a)}{\approx} \left(\sum_{m=1}^M \frac{|a_{m,n}|^2}{\hat{\beta}^{-1} + \bar{v}_m^z} \right)^{-1}, \tag{77}$$

$$\bar{t}_n \stackrel{(c)}{\approx} \hat{t}_n + \bar{v}_n^t \sum_{m=1}^M a_{m,n}^* \frac{r_m - \bar{z}_m}{\hat{\beta}^{-1} + \bar{v}_m^z}, \tag{78}$$

where (a) and (b) are obtained with $\bar{v}_m^z \gg |a_{m,n}|^2 \bar{v}_{n,m}^t$; (c) is obtained with $|a_{m,n}|^2 / (\hat{\beta}^{-1} + \bar{v}_m^z) \ll 1/\hat{v}_n^t$, since $|a_{m,n}|^2 / (\hat{\beta}^{-1} + \bar{v}_m^z) \ll 1/\hat{v}_n^t$ for large M from (77) and $\bar{v}_n^t \geq \hat{v}_n^t$. Similarly, the variance \bar{v}_q^c and mean \bar{c}_q in (40) can be approximated as

$$\bar{v}_q^c \approx \left(\sum_{n=1}^{N_R} \frac{|d_{n,q}|^2}{\bar{v}_n^x + \bar{v}_n^x} \right)^{-1}, \tag{79}$$

$$\bar{c}_q \approx \hat{c}_q + \bar{v}_q^c \sum_{n=1}^{N_R} d_{n,q}^* \frac{\bar{x}_n - \bar{x}_n}{\bar{v}_n^x + \bar{v}_n^x}. \tag{80}$$

F. Overall Algorithm and Complexity Analysis

The proposed three-layer generalized approximate message passing (TL-GAMP) algorithm can be organized in a more succinct form, which is summarized in Algorithm 1 and it can be terminated when it reached a maximum number of iteration or the difference between the estimates of two consecutive iterations is less than a threshold. Once the subchannels $\hat{\mathbf{t}}_l$ for $l = 1, 2, \dots, L$ are obtained, the final channel is estimated as $\hat{\mathbf{H}} = \sum_{l=1}^L \hat{\mathbf{t}}_l \mathbf{a}_T^H(\hat{\psi}_l)$.

In the following, we provide the computational complexity analysis for the TL-GAMP algorithm. The TL-GAMP algorithm requires pre-processing, i.e., performing an economic SVD for \mathbf{A} and unitary transformation, and the complexity is $\mathcal{O}(M^2 N_R)$. It is noted that the pre-processing can be carried out offline, thus, the computational complexity can be overlooked. Examining the TL-GAMP algorithms, it is evident that there is no matrix inversion involved, and the most computationally intensive parts only involve matrix-vector products. Specifically, in the first layer, the complexity of the proposed algorithm is dominated by the computation of \bar{c}_q and \bar{x}_n for all q and n , which requires $\mathcal{O}(N_R Q)$. In the second layer, the complexity is dominated by the computation of π_n^{out} , π_n^{in} , ψ_n^f , ψ_n^b , and $b(s_n)$, which requires $\mathcal{O}(N_R)$. In the third layer, the complexity is dominated by the computation of \bar{t}_n and \bar{z}_m , given by $\mathcal{O}(M N_R)$. Therefore, the complexity of TL-GAMP per iteration is $\mathcal{O}(N_R Q + M N_R)$, which linearly increases with M , N_R , and Q . For comparison, we also provide the overall complexity of Turbo-BOMP [28],

Algorithm 1 Proposed TL-GAMP for subchannel estimation

Input: received vector \mathbf{r} , measurement matrix \mathbf{A} and codebook \mathbf{D} ;

- Initialize:** $\{\bar{v}_q^c, \bar{c}_q, \forall q\}$, $\{\bar{t}_n, \bar{v}_n^t, \hat{t}_n, \hat{v}_n^t, \forall n\}$, $\{\bar{z}_m, \bar{v}_m^z, \forall m\}$, $\xi, \eta, p_{01}, \psi_0^f, \psi_{N_R}^b$ and $\hat{\beta}$.
- 1: **while** the stopping criterion is not met **do**
 - /*The first layer*/
 - 2: Update the posterior estimate of γ_q according to (27), $\forall q \in \mathcal{Q}$;
 - 3: Update the posterior estimate of c_q according to (30), $\forall n \in \mathcal{N}$;
 - 4: Update the output message $m_{f_{x_n} \rightarrow x_n}(x_n)$ of the first layer according to (75) and (76), $\forall q \in \mathcal{Q}$;
 - 5: Update the message from c_q to f_{c_q} according to (79) and (80), $\forall q \in \mathcal{Q}$;
 - /*The second layer*/
 - 6: Update the forward and backward messages of Markov chain according to (45) and (46);
 - 7: Update the output messages of Markov chain according to (44);
 - 8: Update the belief of s_n according to (47), $\forall n \in \mathcal{N}$;
 - 9: Update ψ_0^f of Markov chain according to (49);
 - 10: Update the output message of the second layer to x_n given by $\bar{x}_n = \bar{t}_n$, $\bar{v}_n^x = \bar{v}_n^t$, $\forall n \in \mathcal{N}$;
 - /*The third layer*/
 - 11: Update the message from z_m to f_{z_m} according to (73) and (74), $\forall m \in \mathcal{M}$;
 - 12: Update the posterior estimate of β according to (59);
 - 13: Update the posterior estimate of z_m according to (62), $\forall m \in \mathcal{M}$;
 - 14: Update the message from t_n to f_{t_n} according to (77) and (78), $\forall n \in \mathcal{N}$;
 - 15: Update the posterior estimation of t_n according to (68) and (69).
 - 16: **end while**
 - 17: Calculate \hat{s}_n according to (48).
- Output:** \hat{t}_n, \hat{s}_n , and \hat{c}_q for all n and q .

which is $\mathcal{O}(I_1 M N_R + I_2 N_R Q)$, where I_1 and I_2 denote the number of iterations in stages I and II, respectively. It can be seen that the two algorithms have comparable computational complexity. However, it is important to note that the novel TL-GAMP algorithm exhibits significant performance superiority compared to the Turbo-BOMP algorithm, as will be verified in Section VI.

V. SIMULATION RESULTS

In this section, we evaluate the performance of the proposed channel estimation scheme under various simulations. The system parameters are shown in Table II. In particular,

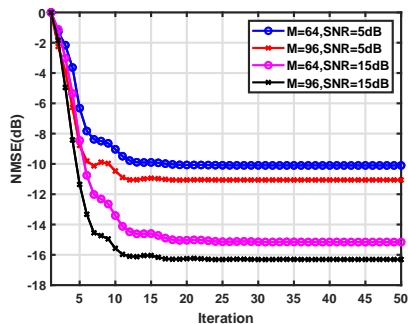


Fig. 8. Convergence performance

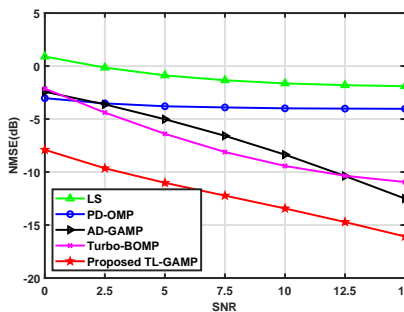
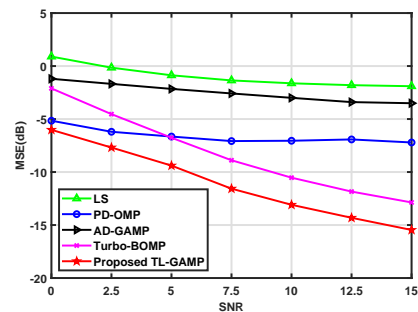
Fig. 9. $\psi_l = 0.25$ for all l .Fig. 10. $\psi_l \in (0,1)$ for all l

TABLE II. Simulation Parameters

Notations	Parameters
Number of BS antennas N_R	256
Number of User antennas N_T	16
Number of RF chains N_{RF}	8
Carrier frequency f_c	30GHz
Number of channel paths L	6
Angle of arrival ϑ_l	$\mathcal{U}(-\pi/2, \pi/2)$
Angle of departure ψ_l	$\mathcal{U}(-\pi/2, \pi/2)$
Distance between BS and UE or scatterers r_l	[10, 50]m
Proportion of visible antenna elements ψ_l	(0,1)
SNR	β
Number of channel realizations	2000

we consider the normalized mean square error (NMSE) as the performance metrics, which is defined as $\text{NMSE} \triangleq \|\hat{\mathbf{H}} - \mathbf{H}\|_{\text{F}}^2 / \|\mathbf{H}\|_{\text{F}}^2$, where \mathbf{H} and $\hat{\mathbf{H}}$ are the true channel and estimated channel, respectively. To effectively evaluate subchannel estimation performance, we compare our proposed TL-GAMP algorithm with the following benchmarks:

- **LS**: Least squares estimator based on the formulation (12). More specifically, the SnS subchannel is estimated as $\mathbf{h}_{l,\text{LS}} = (\mathbf{W}\mathbf{W}^H)^{-1}\mathbf{W}^H\mathbf{y}_l$ for all l .
- **PD-OMP**: On-grid polar-domain simultaneous orthogonal matching pursuit algorithm for near-field channels proposed in [17] without considering the SnS property.
- **AD-GAMP**: Antenna-domain generalized approximate message passing algorithm without utilizing the angular-domain statistical characteristics, which is similar to the methods proposed in [25], [26].
- **Turbo-BOMP**. Two-stage VR detection and channel estimation scheme proposed in our previous work [28], where the angular-domain information can not be utilized in VR detection stage.

We first examine the average convergence behavior of the TL-GAMP algorithm. As shown in Fig. 8, the NMSE exhibits a consistent monotonic reduction across iterations. The convergence of the proposed TL-GAMP algorithm is verified for all the considered simulation scenarios. Considering both performance and computational complexity, the maximum iteration can be safely set as 20 for subsequent simulations.

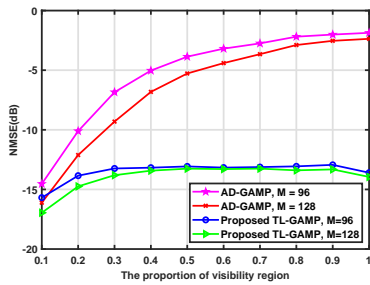
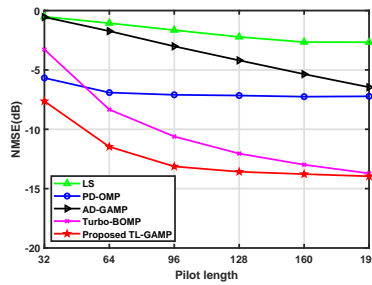
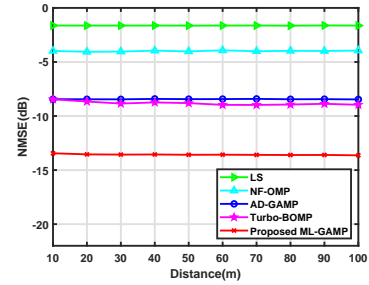
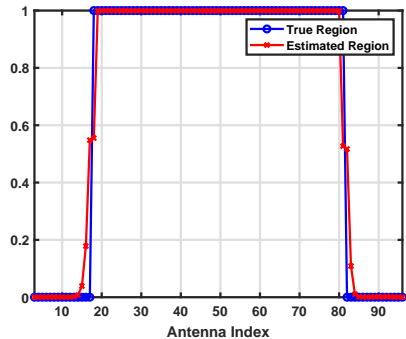
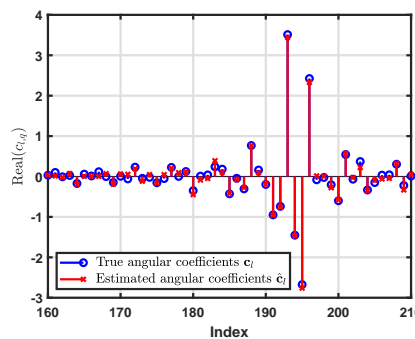
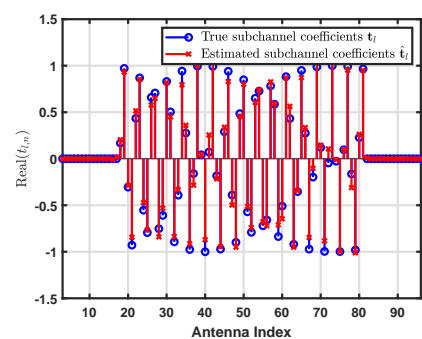
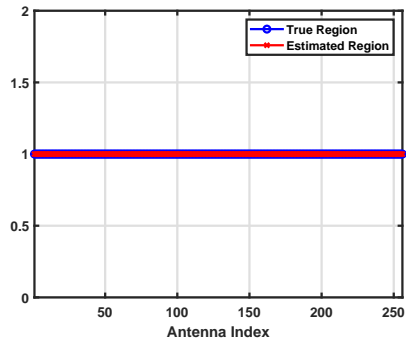
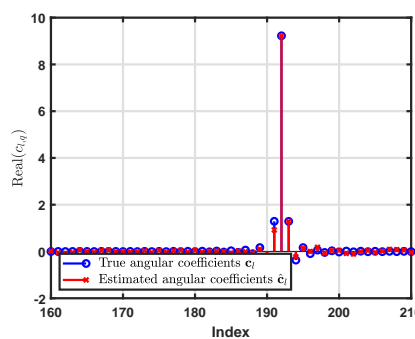
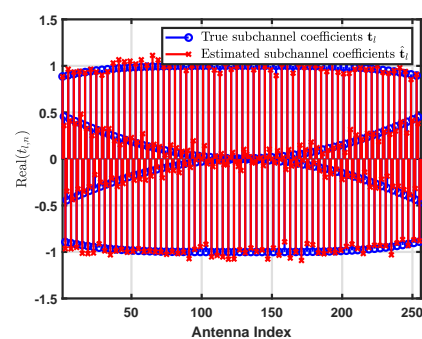
Then, the NMSE performance versus SNR with fixed size of VR, i.e., fixed ϕ_l , is examined, as shown in Fig. 9. It is clear that the conventional near-field channel estimation approaches, such as LS and PD-OMP encounter pronounced performance degradation since the SnS property is not considered. Meanwhile, compared to the existing AD-GAMP and

Turbo-BOMP schemes, our proposed TL-GAMP algorithm exhibits remarkable superiority. To elaborate, in contrast with the AD-GAMP approach, which only utilizes the antenna-domain channel characteristics, our approach concurrently harnesses both antenna-domain and angular-domain channel characteristics, yielding enhanced estimation accuracy. In contrast to the Turbo-BOMP approach, the collaboration between VR detection and angular channel estimation in our proposed TL-GAMP algorithm effectively prevents error propagation. Consequently, the NMSE performance of the TL-GAMP algorithm improves significantly.

Furthermore, we present the NMSE performance versus SNR with $\phi_l \in (0, 1]$, depicted in Fig. 10. Notably, compared to $\phi_l = 0.25$, a notable observation emerges: the AD-GAMP method experiences a substantial performance drop, while the proposed TL-GAMP algorithm's performance remains nearly unchanged. This divergence in performance can be attributed to the AD-GAMP algorithm's reliance on the sparsity of the antenna domain. Consequently, as the VR expands, the antenna domain's sparsity diminishes, leading to a consequential performance degradation. In contrast, the proposed TL-GAMP algorithm shows commendable robustness to varying ϕ_l . To further substantiate this observation, Fig. 11 plots the NMSE performance against ϕ_l with $M = 96$ and $\text{SNR} = 10\text{dB}$, it is clear that the performance of the proposed TL-GAMP only exhibits slight fluctuation as ϕ_l , which means that the joint utilization of statistical characteristics in antenna and angular domain significantly improve the algorithm robustness for the size of VR. As a result, the proposed TL-GAMP is suitable for both spatially stationary and SnS scenarios.

Furthermore, the performance comparison of the proposed TL-GAMP algorithm and the benchmarks with different pilot length M is evaluated in Fig. 12 with $\text{SNR} = 10\text{dB}$ and $\phi_l \in (0, 1]$ for all l . The pilot length M increases from 32 to 192. It is observed that the performance of all algorithms keep improving when pilot length M increases. However, the performance improvement diminishes as M keeps increasing, and eventually the performance saturates. As such, we can set a moderate value M to take a compromise between performance and estimation delay. Furthermore, we can also see that the proposed TL-GAMP algorithms significantly outperform the existing algorithms, especially when the pilot length is small. This indicates that the proposed algorithms can significantly reduce the overhead for SnS XL-MIMO channel estimation.

Fig. 13 depicts the NMSE performance concerning the

Fig. 11. NMSE performance versus ϕ_l Fig. 12. NMSE performance versus M .Fig. 13. NMSE performance versus r_l (a) VR detection probability $b(s_l)$.(b) Angular-domain coefficients \hat{c}_l (c) Antenna-domain coefficients \hat{t}_l Fig. 14. Near-field SnS scenarios with $M = 96$ and $SNR = 15$ dB.(a) VR detection probability $b(s_l)$.(b) Angular-domain coefficients \hat{c}_l (c) Antenna-domain coefficients \hat{t}_l Fig. 15. Far-field spatially stationary scenarios with $M = 96$ and $SNR = 15$ dB.

distance between the BS and either the scatterers or the user, with fixed values of $M = 96$ and $SNR = 10$ dB. Notably, the results indicate robustness across all algorithms in response to varying distances. However, it is noteworthy that the proposed TL-GAMP algorithm significantly outperforms the benchmark methods in the considered configurations. Furthermore, the demonstrated robustness across varying distances highlights a key attribute of our proposed channel estimation scheme: its feasibility in both near-field and far-field settings.

Finally, the estimation performance of the involved intermediate quantities are presented including the VR detection probability denoted as $b(s_l)$, the estimated angular channel coefficients \hat{c}_l , and the estimated subchannel coefficients \hat{t}_l . From Fig. 14 and Fig. 15, it can be observed that across various conditions, including far-field and near-field scenarios, as well as both spatial stationary and SnS scenarios, the proposed algorithm consistently exhibits the capability to robustly detect

the visible region and accurately estimate the corresponding channel coefficients.

VI. CONCLUSION AND FUTURE WORKS

In this work, we have studied the SnS channel estimation problem for the XL-MIMO systems and proposed a two-phase channel estimation scheme capable of efficiently recovering channels. Initially, to decouple multiple propagation paths, we first estimate the AoDs of the user, followed by the estimation of individual subchannels. The problem of subchannel estimation is formulated as a three-layer generalized bilinear inference problem. To achieve the inference with low computational complexity, we propose a computationally efficient TL-GAMP algorithm by exploiting both the antenna-domain and angular-domain characteristics of SnS channels. Simulation results show that the proposed algorithm can achieve much better NMSE performance than the existing algorithms with

reduced pilot overhead. Furthermore, the algorithm exhibits robustness to different channel scenarios. Looking ahead, future research may involve concurrent estimation of multiple paths to further reduce training overhead and the optimization of combining matrices. Additionally, there is potential to extend the proposed TL-GAMP method to double-side XL-MIMO channel estimation with SnS property.

REFERENCES

- [1] X. You, C.-X. Wang, J. Huang, X. Gao, Z. Zhang, M. Wang, Y. Huang, C. Zhang, Y. Jiang, J. Wang *et al.*, "Towards 6G wireless communication networks: Vision, enabling technologies, and new paradigm shifts," *Sci. China Inf. Sci.*, vol. 64, pp. 1–74, 2021.
- [2] H. Tataria, M. Shafi, A. F. Molisch, M. Dohler, H. Sjlund, and F. Tufvesson, "6G wireless systems: Vision, requirements, challenges, insights, and opportunities," *Proc. IEEE*, vol. 109, no. 7, pp. 1166–1199, 2021.
- [3] Z. Wang, J. Zhang, H. Du, W. E. I. Sha, B. Ai, D. Niyato, and M. Debbah, "Extremely large-scale MIMO: Fundamentals, challenges, solutions, and future directions," *IEEE Wirel. Commun.*, pp. 1–9, 2023.
- [4] M. Cui, Z. Wu, Y. Lu, X. Wei, and L. Dai, "Near-field MIMO communications for 6G: Fundamentals, challenges, potentials, and future directions," *IEEE Commun. Mag.*, vol. 61, no. 1, pp. 40–46, 2023.
- [5] D. Dardari and N. Decarli, "Holographic communication using intelligent surfaces," *IEEE Commun. Mag.*, vol. 59, no. 6, pp. 35–41, 2021.
- [6] Z. Zhang and L. Dai, "Pattern-division multiplexing for multi-user continuous-aperture MIMO," *IEEE J. Sel. Areas Commun.*, vol. 41, no. 8, pp. 2350–2366, 2023.
- [7] A. Tang, J.-B. Wang, Y. Pan, W. Zhang, Y. Chen, H. Yu, and R. C. de Lamare, "Line-of-sight extra-large MIMO systems with angular-domain processing: Channel representation and transceiver architecture," *IEEE Trans. Commun.*, vol. 72, no. 1, pp. 570–584, 2024.
- [8] Y. Pan, C. Pan, S. Jin, and J. Wang, "RIS-aided near-field localization and channel estimation for the terahertz system," *IEEE J. Sel. Topics Signal Process.*, vol. 17, no. 4, pp. 878–892, 2023.
- [9] K. T. Selvan and R. Janaswamy, "Fraunhofer and fresnel distances: Unified derivation for aperture antennas," *IEEE Antennas Propag. Mag.*, vol. 59, no. 4, pp. 12–15, 2017.
- [10] H. Lu and Y. Zeng, "Communicating with extremely large-scale array/surface: Unified modeling and performance analysis," *IEEE Trans. Wireless Commun.*, vol. 21, no. 6, pp. 4039–4053, 2022.
- [11] E. Björnson and L. Sanguinetti, "Power scaling laws and near-field behaviors of massive MIMO and intelligent reflecting surfaces," *IEEE open J. Commun. Soc.*, vol. 1, pp. 1306–1324, 2020.
- [12] Y. Han, S. Jin, C.-K. Wen, and T. Q. S. Quek, "Localization and channel reconstruction for extra large RIS-assisted massive MIMO systems," *IEEE J. Sel. Topics Signal Process.*, vol. 16, no. 5, pp. 1011–1025, 2022.
- [13] K. Zhi, C. Pan, H. Ren, K. K. Chai, C.-X. Wang, R. Schober, and X. You, "XL-MIMO with near-field spatial non-stationarities: Low-complexity detector design," in *2023 IEEE Glob. Commun. Conf.*, 2023, pp. 7194–7199.
- [14] Z. Yuan, J. Zhang, Y. Ji, G. F. Pedersen, and W. Fan, "Spatial non-stationary near-field channel modeling and validation for massive MIMO systems," *IEEE Trans. Antennas Propag.*, vol. 71, no. 1, pp. 921–933, 2023.
- [15] E. D. Carvalho, A. Ali, A. Amiri, M. Angjelichinoski, and R. W. Heath, "Non-stationarities in extra-large-scale massive MIMO," *IEEE Wirel. Commun.*, vol. 27, no. 4, pp. 74–80, 2020.
- [16] J. Flordelis, X. Li, O. Edfors, and F. Tufvesson, "Massive MIMO extensions to the COST 2100 channel model: Modeling and validation," *IEEE Trans. Wireless Commun.*, vol. 19, no. 1, pp. 380–394, 2020.
- [17] M. Cui and L. Dai, "Channel estimation for extremely large-scale MIMO: Far-field or near-field?" *IEEE Trans. Commun.*, vol. 70, no. 4, pp. 2663–2677, 2022.
- [18] W. Liu, H. Ren, C. Pan, and J. Wang, "Deep learning based beam training for extremely large-scale massive MIMO in near-field domain," *IEEE Commun. Lett.*, vol. 27, no. 1, pp. 170–174, 2023.
- [19] Y. Zhang, X. Wu, and C. You, "Fast near-field beam training for extremely large-scale array," *IEEE Wireless Commun. Lett.*, vol. 11, no. 12, pp. 2625–2629, 2022.
- [20] X. Wei and L. Dai, "Channel estimation for extremely large-scale massive MIMO," *IEEE Commun. Lett.*
- [21] Z. Hu, C. Chen, Y. Jin, L. Zhou, and Q. Wei, "Hybrid-field channel estimation for extremely large-scale massive MIMO system," *IEEE Commun. Lett.*, vol. 27, no. 1, pp. 303–307, 2023.
- [22] Y. Han, S. Jin, C.-K. Wen, and X. Ma, "Channel estimation for extremely large-scale massive MIMO systems," *IEEE Wireless Commun. Lett.*, vol. 9, no. 5, pp. 633–637, 2020.
- [23] Y. Chen and L. Dai, "Non-stationary channel estimation for extremely large-scale MIMO," *IEEE Trans. Wireless Commun.*, pp. 1–15, 2023, early access, doi: [10.1109/TWC.2023.3343740](https://doi.org/10.1109/TWC.2023.3343740).
- [24] X. Cheng, K. Xu, J. Sun, and S. Li, "Adaptive grouping sparse bayesian learning for channel estimation in non-stationary uplink massive MIMO systems," *IEEE Trans. Wireless Commun.*, vol. 18, no. 8, pp. 4184–4198, 2019.
- [25] H. Iimori, T. Takahashi, K. Ishibashi, G. T. F. de Abreu, D. Gonzalez G., and O. Gonsa, "Joint activity and channel estimation for extra-large MIMO systems," *IEEE Trans. Wireless Commun.*, vol. 21, no. 9, pp. 7253–7270, 2022.
- [26] Y. Zhu, H. Guo, and V. K. N. Lau, "Bayesian channel estimation in multi-user massive MIMO with extremely large antenna array," *IEEE Trans. Signal Process.*, vol. 69, pp. 5463–5478, 2021.
- [27] X. Yu, W. Shen, R. Zhang, C. Xing, and T. Q. S. Quek, "Channel estimation for XL-RIS-aided millimeter-wave systems," *IEEE Trans. Commun.*, vol. 71, no. 9, pp. 5519–5533, 2023.
- [28] A. Tang, J.-B. Wang, Y. Pan, W. Zhang, Y. Chen, H. Yu, and R. C. De Lamare, "Joint Visibility Region and Channel Estimation for Extremely Large-scale MIMO Systems," *arXiv e-prints*, p. arXiv:2311.09490, Nov. 2023.
- [29] J. Gao, C. Zhong, G. Y. Li, J. B. Soriaga, and A. Behboodi, "Deep learning-based channel estimation for wideband hybrid mmwave massive MIMO," *IEEE Trans. Commun.*, vol. 71, no. 6, pp. 3679–3693, 2023.
- [30] J. Wu, S. Kim, and B. Shim, "Parametric sparse channel estimation for RIS-assisted terahertz systems," *IEEE Trans. Commun.*, pp. 1–1, 2023.
- [31] J. He, H. Wymeersch, and M. Juntti, "Channel estimation for RIS-aided mmwave MIMO systems via atomic norm minimization," *IEEE Trans. Wireless Commun.*, vol. 20, no. 9, pp. 5786–5797, 2021.
- [32] Z. Yang and L. Xie, "Exact joint sparse frequency recovery via optimization methods," *IEEE Trans. Signal Process.*, vol. 64, no. 19, pp. 5145–5157, 2016.
- [33] T. Ma, Y. Xiao, and X. Lei, "Channel reconstruction-aided MUSIC algorithms for joint AoA and AoD estimation in MIMO systems," *IEEE Wireless Commun. Lett.*, vol. 12, no. 2, pp. 322–326, 2023.
- [34] A. Liao, Z. Gao, H. Wang, S. Chen, M.-S. Alouini, and H. Yin, "Closed-loop sparse channel estimation for wideband millimeter-wave full-dimensional MIMO systems," *IEEE Trans. Commun.*, vol. 67, no. 12, pp. 8329–8345, 2019.
- [35] Z. Yuan, Q. Guo, and M. Luo, "Approximate message passing with unitary transformation for robust bilinear recovery," *IEEE Trans. Signal Process.*, vol. 69, pp. 617–630, 2021.
- [36] Y. Guo, P. Sun, Z. Yuan, C. Huang, Q. Guo, Z. Wang, and C. Yuen, "Efficient channel estimation for RIS-aided MIMO communications with unitary approximate message passing," *IEEE Trans. Wireless Commun.*, vol. 22, no. 2, pp. 1403–1416, 2023.
- [37] Q. Zou, H. Zhang, and H. Yang, "Multi-layer bilinear generalized approximate message passing," *IEEE Trans. Signal Process.*, vol. 69, pp. 4529–4543, 2021.
- [38] L. Mo, X. Lu, J. Yuan, C. Zhang, Z. Wang, and P. Popovski, "Generalized unitary approximate message passing for double linear transformation model," *IEEE Trans. Signal Process.*, vol. 71, pp. 1524–1538, 2023.
- [39] S. Rangan, "Generalized approximate message passing for estimation with random linear mixing," in *2011 IEEE Int. Symp. Inf. Theor. Proc.*, 2011, pp. 2168–2172.
- [40] P. Schniter and S. Rangan, "Compressive phase retrieval via generalized approximate message passing," *IEEE Trans. Signal Process.*, vol. 63, no. 4, pp. 1043–1055, 2015.
- [41] R. B. Di Renna and R. C. de Lamare, "Joint channel estimation, activity detection and data decoding based on dynamic message-scheduling strategies for mMTC," *IEEE Trans. Commun.*, vol. 70, no. 4, pp. 2464–2479, 2022.
- [42] S. Rangan, P. Schniter, and A. K. Fletcher, "Vector approximate message passing," *IEEE Trans. Inf. Theory*, vol. 65, no. 10, pp. 6664–6684, 2019.
- [43] W. Zhu, M. Tao, X. Yuan, and Y. Guan, "Message passing-based joint user activity detection and channel estimation for temporally-correlated massive access," *IEEE Trans. Commun.*, vol. 71, no. 6, pp. 3576–3591, 2023.